AN ABSTRACT OF THE THESIS OF

Eric M. Walters for the degree of Master of Science in Mechanical Engineering
presented on July 25, 2016.

Title: Stability and Liftoff of Non-premixed Large Hydrocarbon Flames in MILD
Conditions

Abstract approved: _____

David L. Blunck

The Moderate or Intense Low-oxygen Dilution (MILD) combustion regime has received interest from the industrial furnace and gas turbine engine industries due to attractive properties of reduced NO_x emissions and high thermal efficiency. MILD combustion is characterized by low oxygen concentrations (i.e. 3%-9% by volume) and high reactant temperatures. A fundamental understanding of the physics governing MILD combustion is required to design effective practical combustion devices. While the physics relevant to MILD combustion of small hydrocarbon fuels such as methane and ethylene have been well-characterized, the behavior of large hydrocarbon fuels, such as Jet-A, have not. This is significant because many practical devices such as internal combustion engines and gas turbine engines are designed to operate using large hydrocarbon fuels. With this background and motivation, the focus of the current study was to understand the mechanisms

governing stability and ignition of these flames in the MILD regime.

To this end, a series of experimental and numerical studies were conducted to identify the physics governing lifted large hydrocarbon flames in the MILD regime. A jet in hot coflow (JHC) burner was used to stabilize a large hydrocarbon flame in a laboratory environment. The coflow used a premixed CH_4/H_2 secondary burner to provide an oxidizer stream at high temperature and with low oxygen concentration, which emulates MILD conditions. The coflow temperature was varied between 1300K and 1500K and the oxygen concentration was varied between 3% and 9% by volume. Three different large hydrocarbon fuels (i.e. Jet-A and two experimental fuels) were vaporized and issued into the hot coflow, with Reynolds numbers based on the inner jet diameter ranging from 3,750 to 10,000. The fuel jet exit temperature was varied from 525K to 625K. The liftoff heights of the resulting flames were measured using OH* chemiluminescence, as the flames were not always visible. Opposed flow laminar diffusion flames simulations were employed to determine how the interaction between chemistry and strain may affect flame stability. Ignition delay calculations were used to determine how ignition chemistry may affect flame liftoff without considering the effect of mixing.

Several conclusions were made from the measurements and simulations. Oscillation of the instantaneous flame liftoff height was observed and was attributed to the cyclic advection of burned fluid downstream and the subsequent autoignition of unburned fluid. An increase in the fuel jet temperature was found to stabilize the flames closer to the jet exit, which was attributed to an increase in entrainment caused by higher fuel jet velocities. Flames in a coflow with 3% O_2 at an

exit temperature of 1300K were found to exhibit a decrease in liftoff height with increasing fuel jet Reynolds number. This counter-intuitive trend was not observed in flames burning in a coflow with higher temperatures or in coflows with higher O_2 concentrations. The decrease in flame liftoff height with Reynolds number was attributed to the transport of formaldehyde into unburned mixture via the observed oscillations in the flame base. This conclusion was supported by both PLIF measurements performed by previous researchers on gaseous MILD flames and by numerical calculations. Opposed flame simulations indicated that formaldehyde production was increased with strain rate, which is analogous to an increase in the fuel jet velocity. Ignition delay calculations indicated that formaldehyde addition decreased ignition delay times, which results in lower flame liftoff heights. Opposed flow flame simulations indicated that the effect of changes in CH_2O production was diminished at increased coflow oxygen levels (i.e. 6% and 9%) and elevated coflow temperatures (i.e. 1400K and 1500K) due to lower formaldehyde production.

Stability and Liftoff of Non-premixed Large Hydrocarbon Flames in
MILD Conditions

by

Eric M. Walters

A THESIS

submitted to

Oregon State University

in partial fulfillment of
the requirements for the
degree of

Master of Science

Presented July 25, 2016
Commencement June 2017

Master of Science thesis of Eric M. Walters presented on July 25, 2016.

APPROVED:

_____

Major Professor, representing Mechanical Engineering

_____

Head of the School of Mechanical, Industrial, and Manufacturing Engineering

_____

Dean of the Graduate School

I understand that my thesis will become part of the permanent collection of Oregon State University libraries. My signature below authorizes release of my thesis to any reader upon request.

_____

Eric M. Walters, Author

ACKNOWLEDGEMENTS

I would first like to express my sincere thanks to my advisor, Dr. David Blunck. I have grown much as both a scientist and as a person thanks to his guidance, support, and trust.

I would like to thank Dr. Hai Wang for providing the chemical kinetic mechanisms for large hydrocarbon fuels and Dr. Tim Edwards for providing the fuels.

I would also like to thank Dr. Nancy Squires for her generous donation of personal time to teach and mentor students and inspire them to push the envelope in all aspects of their life. Her guidance, kindness, and always cheerful attitude have helped me immeasurably during my time at OSU.

Many thanks to Alex Bruzda, who was instrumental in collecting quality data and providing a fresh perspective into challenging research problems.

I could not have accomplished all I have done without my family, including my parents Jan and John and my brother Ian. They have always been there for me and I know they always will.

Lastly, I would like to thank all of my friends, who made my college experience the best it could have possibly been. I will never forget the fun we all had together.

TABLE OF CONTENTS

TABLE OF CONTENTS (Continued)

LIST OF FIGURES

LIST OF TABLES

LIST OF APPENDICES

LIST OF APPENDIX FIGURES

LIST OF APPENDIX TABLES

This thesis is dedicated to Emma McGuiness, who selflessly poured her heart and soul into supporting me through my graduate program. I thank her from the bottom of my heart for her patience and love.

Chapter 1: Introduction

1.1   Motivation and Background

New combustion technologies are desired to reduce pollutant emissions in energy conversion devices. Reduction of NO_x formation without compromising combustion efficiency has proven challenging. High preheat temperatures enable near complete conversion of CO into CO_2, but exacerbate thermal NO_x production through the Zeldovich mechanism [2]. It has been found that through strong exhaust gas recirculation, air preheat and dilution is achieved while the maximum flame temperature is reduced due to dilution of the reactants with combustion products. Under these conditions, thermal NO_x formation is suppressed [3]. When the reactant preheat temperature exceeds the mixture autoignition temperature and the local oxygen concentration is reduced below about 12% by volume, the resulting reaction is considered to be moderate or intense low-oxygen dilution (MILD) combustion [4, 5].

MILD combustion has several advantages in practical combustion devices. Diluting reactants with combustion products generates a spatially distributed reaction front [6]. Producing more uniform heat release over a relatively large area increases the service life of high temperature furnaces by preventing the formation of hot spots that degrade combustor liners. A MILD reaction zone is self-stabilizing

because the reactant temperatures are above autoignition, allowing a large degree of flexibility in the reactant injection strategy and fluid flow path through the burner [7]. In addition, the long residence times produced by recirculating exhaust products provides sufficient time for near complete conversion of CO into CO_2 [8]. Both NO_x and CO emissions can be reduced in a MILD environment compared to conventional combustion, where typically a tradeoff between production of these two pollutants is required. With these attractive properties, MILD combustion has garnered considerable interest for implementation in industrial furnaces [9], gas turbine engines [10], and homogeneous charge compression ignition engines [4].

The physics governing the structure and stability of MILD conditions are still poorly understood, hindering widespread implementation of MILD combustion technologies. Fundamental studies are required to ascertain important design criteria for the successful implementation of MILD combustion devices. While significant work has been done on the stability characteristics of small hydrocarbon fuels such as methane and ethylene in the MILD regime, the literature available for the MILD combustion characteristics of pre-vaporized large hydrocarbon fuels is comparatively sparse. Most of these studies have focused on the implementation of large hydrocarbon MILD combustion in practical burners [11–13], not the physics that control liftoff and stability in these flames. The high energy density of large hydrocarbon fuels makes them an attractive choice where compact storage is required, such as automotive or aerospace applications. Large hydrocarbons may provide advantages over small hydrocarbons in other applications, as the droplet

evaporation kinetics of large hydrocarbons can extend the stable operating range of MILD burners originally designed for gaseous fuels [14]. The combustion chemistry of long-chain hydrocarbons is substantially more complex than that of small hydrocarbon fuels [15], and may lead to differences in the reaction zone structure and flame stability [16]. The structure and stability characteristics of these flames must be characterized in order to help design practical MILD combustors to run on large hydrocarbon fuels.

1.2 Objectives

With this motivation and background, the purpose of this work is to examine the stability characteristics of large hydrocarbon fuels in a MILD environment. A number of parameters thought to be vital in the stabiliation of lifted flames in MILD conditions will be varied to assess their effect on the flame liftoff height. It is important to characterize any regions of reduced flame stability, which could impact the design of practical burners. For example, DeJoannon et al. [17] discovered a narrow set of temperature, pressure, and oxygen concentration conditions in the MILD regime that were found to cause flame instabilities. The cause of this unstable region was not identified. No such survey has been performed using large hydrocarbons in the MILD regime. This work will attempt to identify any similar instability singularities which will compromize practical combustor designs if they are not accounted for.

The objectives of this work are as follows:

1. Identify the influence of oxygen concentration on the liftoff characteristics of large hydrocarbon flames in a MILD environment.

2. Identify changes in the physical and chemical processes governing flame liftoff as the fuel temperature of large hydrocarbon MILD flames is changed.

3. Ascertain the effect of oxidant stream temperature on the liftoff heights of large hydrocarbon flames in a MILD environment

Chapter 2: Literature Review

2.1   Small Hydrocarbon Flames in a Hot and Diluted Coflow

Significant experimental work investigating the combustion characteristics of small hydrocarbon flames in the MILD regime has been conducted using a jet in hot coflow (JHC) burner geometry [5, 6, 18–21]. The same geometry will be employed in the current work and is discussed in Section 3.1. The burner was originally developed by Dally et al. [18] to study MILD combustion using laser diagnostics in an optically-accessible environment. Unrestricted optical access is difficult to obtain in conventional MILD burners, as an enclosed space is typically employed to develop exhaust gas recirculation that produces the low oxygen concentrations and high reactant temperatures required for MILD combustion. The JHC burner overcomes this problem by using an annular secondary burner to generate a hot oxidizer stream that contains combustion products, nitrogen, and an oxygen concentration of 3-12% by volume. Fuel is fed into the hot annular stream from an concentric insulated tube, which emulates MILD combustion in a non-premixed jet flame.

Several research efforts have since used the JHC burner design to study MILD combustion of gaseous fuels using a variety of optical diagnostic techniques. Examples of these techniques include OH and CH_2O Planar Laser-Induced Fluorescence

(PLIF) [6, 22], Rayleigh temperature measurements [6, 22], OH* and CH* chemi-luminescence [20, 21, 23], and high speed photography [24, 25]. The research efforts of Dr. Paul Medwell of the University of Adelaide have provided a detailed understanding of the combustion process in small hydrocarbon flames stabilized by the JHC burner and deserves significant attention in this review.

Medwell obtained simultaneous measurements of OH, formaldehyde (CH_2O), and temperature distributions using laser imaging techniques on a flame using a mixture of CH_4 and H_2 in a 1:1 volumetric ratio. The coflow temperature was fixed at 1100K and the oxygen concentration varied between 3% and 9% by volume. The flame structure was found to be typified by strong formaldehyde (CH_2O) signals in the fuel-rich region of the jet bordered by an OH layer at the interface between the jet and the coflow [22]. The OH radical is commonly used as a qualitative indicator for flame location [26]. A localized reaction zone weakening phenomena was observed in flames with a 3% O_2 concentration in the coflow, as indicated by faint OH signals. Evidence of local extinction was not found, as the OH layer remained intact. However, weakening of the reaction zone allowed CH_2O from the fuel-rich region to penetrate the OH layer. The frequency of weakening events was found to increase with the fuel jet Reynolds number. The phenomena was investigated further in a later publication, which found evidence of significant partial premixing due to the weakened reaction zone [27]. Partial premixing was found to play an important role in the stabilization of MILD flames. Reaction zone weakening could play an important role in large hydrocarbon flames and will be discussed later.

In another study, Medwell applied the same measurement techniques to ethylene flames under similar coflow conditions [28]. The flames initially appeared to be lifted, but examination of the apparent flame base revealed the presence of a weaker reaction that extended to the jet exit plane. The location of this apparent liftoff height moved upstream as the fuel jet Reynolds number was increased. This trend was unexpected, as flame liftoff heights generally increase with Reynolds number in conventional flames [29, 30]. The behavior was attributed to increased mixing near the jet exit, which reduces the time required for ignition to occur (commonly referred to as ignition delay time). Medwell suggested further research into this area, as the phenomena was not fully understood. It is possible that a similar phenomena may occur in large hydrocarbon flames.

A numerical study was performed by Medwell to investigate the role of formaldehyde and other flame radicals in MILD combustion [20]. Opposed flow laminar diffusion flame calculations using a high temperature oxidizer stream with low O_2 concentrations revealed that formaldehyde concentrations are significantly enhanced with increasing strain rate. The O_2 concentration at the location of peak formaldehyde, which occurs on the fuel-rich side of the flame, was also found to increase with strain rate. Penetration of O_2 into the fuel-rich side of the flame was greatly enhanced when the oxidizer stream contained less O_2 (i.e. 3% by volume), which is consistent with the evidence of partial premixing discussed in [27]. Ignition delay calculations also revealed that the addition of CH_2O to the unburned mixture significantly reduced ignition delay times (i.e. by up to 90% for a 1% volumetric concentration of CH_2O) for all simulated conditions. Formaldehyde

addition was found to reduce ignition delay times the most in mixtures with the lowest oxygen concentration (i.e. 3% by volume), indicating that the role of CH_2O on ignition is enhanced in low oxygen conditions. These results were corroborated experimentally, as addition of CH_2O to the fuel stream in a lifted methane JHC flame significantly reduced the liftoff height [20]. It is anticipated that fuel chemistry could substantially affect CH_2O production rates in large hydrocarbon flames, which could affect flame stability.

2.2   Stabilization Mechanisms of Lifted Turbulent Jet Flames

2.2.1   Flame Stabilization in Ambient Air or in a Cold Coflow

Ensuring flame stability over a range of operating conditions is an important design consideration in conventional combustion applications [31]. While burner or bluff body-stabilized flames are often used, it is sometimes desirable to employ a lifted flame design to lessen thermal wear on burner structures [32]. The axial location where stable ignition occurs depends heavily on complex turbulent-chemistry interaction, heat transfer, and the burner geometry. Lifted jet flames in ambient environments or room temperature coflows have been extensively studied and a number of well-developed theories exist regarding the physics involved in stabilizing these flames [33–37]. Flame liftoff height generally increases with jet Reynolds number [29, 30], which agrees with the well-established premixing theory of Vanquickenborne and Van Tiggelen [38]. The premixing theory proposes that a lifted

turbulent diffusion flame will stabilize where the local fluid velocity is equal to the maximum turbulent burning velocity. This theory has been found to show good agreement with many experiments [32], although in some conditions other phenomena can become more important to flame stabilization. Kelvin-Helmholtz instabilities formed by the jet shear layer are thought to be crucial to flame stabilization less than 40 jet radii above the burner, where the local velocity can be significantly higher than the laminar burning velocity [35]. It is hypothesized that large eddies transport heat downstream, where it diffuses into the surrounding slow-moving air and can ignite subsequent eddies [39]. While research is still ongoing in conventional lifted flames, the understanding of the physics involved is considered to be mature. This is not the case for lifted MILD flames, which have only garnered considerable research interest within the last 5-10 years.

2.2.2   Flame Stabilization in MILD Environments

Recent research has highlighted different physical mechanisms governing lifted small hydrocarbon jet flames in hot and diluted coflows. These conditions can emulate those of MILD combustion. The liftoff height of a methane jet in hot coflow flame studied by Medwell [19] was found to initially increase with coflow temperatures (e.g. 1300K to 1400K) and then decrease as the temperature was increased further (e.g. 1400K to 1500K), indicating a transitional behavior in the ignition mechanism. Medwell attributed the trend to a transition from conventional to MILD combustion conditions, but suggested further research to develop

a more detailed understanding of the phenomena.

Oldenhof et al. [24] observed the formation of ignition kernels at the base of MILD combustion of natural gas that grew and were convected downstream. The existence of discrete flame pockets points to a very different ignition mechanism than seen in lifted flames issuing into a cold colfow, where the flame base is sharply defined and no kernels are observed. A similar phenomena was observed in MILD methane flames by Ramachandran [40], where the cyclical formation and growth of ignition kernels caused the flame front to oscillate sporadically. While experiments have agreed that MILD-like jet flames exhibit unique ignition phenomena, the physics involved remain poorly understood.

2.3 MILD Combustion of Large Hydrocarbon Fuels

It is important to acknowledge and learn from the contributions of previous research efforts in the area of large hydrocarbon fuels in the MILD combustion regime. Weber et al. [41] performed a series of measurements on a MILD furnace using natural gas, light fuel oil, and heavy fuel oil to evaluate the differences between fuels. It was found that light fuel oil behaved very similarly to natural gas, but heavy fuel oil produced both visible differences in the flame and increased NO_x production. The reasons for the difference was not well understood, underscoring the importance of understanding how large hydrocarbons behave in MILD conditions. Derudi et al. [14] developed a dual-nozzle burner that established MILD conditions using a gaseous fuel burner. Large hydrocarbon fuels (n-octane,

i-octane, and n-decane) were injected into the MILD flame, where the impact of inlet conditions on sustainability of the MILD combustion environment were assessed. The results were compared to a second study using small hydrocarbon fuels in the same configuration. It was found that large hydrocarbon fuels extended the operating conditions where MILD combustion could be sustained, and NO_x/soot pollutant formation was below acceptable levels. Derudi suggested that the increased operating condition range would allow liquid waste and low-BTU fuels to sustain MILD combustion reactions, even when the feedstock composition was varied.

Ye et al. [16] conducted a parametric study on the qualitative stability and emissions of premixed large hydrocarbon MILD combustion by varying the fuel type, equivalence ratio, carrier gas, operating pressure, and air jet velocity. The joint regime of low CO and low NO_x was found to narrow with an increase in pressure, highlighting the need to understand the formation of these pollutants in high pressure MILD combustion such as in a gas turbine engine combustor. Stability of the reaction was found to be most strongly influenced by the fuel type, with n-heptane appearing less stable than either ethanol or acetone due to faster ignition characteristics at high pressure. Ignition delay times were found to significantly influence the stability of these MILD reactions, as ignition sometimes occurred before the fuel and oxidizer were adequately mixed. Ignition delays of large hydrocarbons in low oxygen environments at high pressure were also studied by De Joannon et al. [17]. Ignition delay times were found to obey a power law as a function of oxygen concentration, with the power being a function of temperature.

The power was found to change non-monotonically for an increasing temperature, and a narrow region of relatively long ignition delay times was found in high pressure conditions. While many of the flames covered in this review are said to be stabilized by autoignition phenomena, there are still a number of uncertainties and wide variations in behavior depending on inlet conditions and fuel type that must be quantified for implementation of large hydrocarbon MILD combustion in practical devices. To the writer's knowledge, no fundamental study on the stabilization mechanisms of lifted large hydrocarbon flames using practical aviation fuels has been performed.

Chapter 3: Experimental Approach

3.1 Burner Design

The jet in hot coflow (JHC) burner used by Dally, Medwell, and others [18, 22, 27, 28, 42–44] to study MILD combustion of gaseous fuels was adapted for the study of non-premixed large hydrocarbon fuels. The burner emulates exhaust gas recirculation in MILD furnaces (using heated and diluted coflow) while providing optical access for non-intrusive measurements. The burner consists of a central fuel jet (ID = 4.6 mm) surrounded by a hot annular coflow (ID = 83.3 mm) as seen in Figure 3.1.

Vaporized fuel issues out of the central jet into the hot, reduced oxygen environment (i.e. 3-9% by volume) created by a secondary burner. The secondary burner is located 150 mm upstream of the jet exit plane and provides a highly diluted oxidant stream at a temperature between 1200K and 1500K at a velocity of approximately 2.3 m/s. A mixture of methane, hydrogen, air, and nitrogen are fed into the secondary burner to produce the desired outlet conditions, which are detailed in Table 3.4. The volumetric oxygen concentration in the coflow exhaust is varied between 3% and 9% (based on equilibrium calculations of the burner inlet composition) while keeping the temperature at the exit plane constant by altering the balance of air and N_2 in the coflow stream. The methane and hydrogen
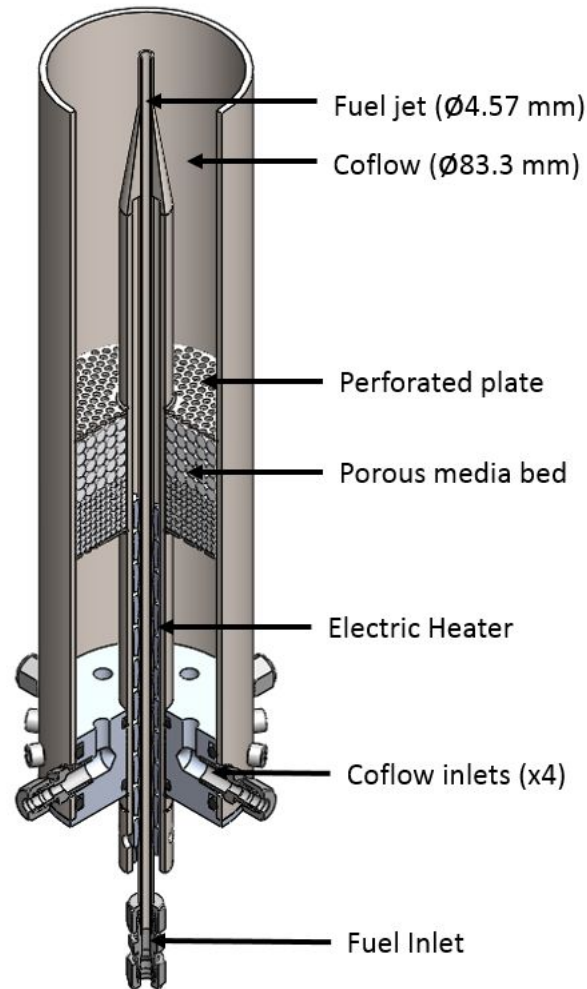
Figure 3.1: Schematic of Modified JHC Burner

flowrates remain unchanged, ensuring that the outlet H_2O and CO_2 volumetric concentrations remain constant at 10% and 3%, respectively. Only the N_2 and O_2 concentrations are altered. The secondary burner inlet conditions are described in Table 3.3. Two layers of alumina spheres ($D_1 = 3$ mm, $D_2 = 6$ mm) stabilize the secondary flame, which must be able to operate at relatively low equivalence

ratios ($\Phi < 0.6$). The porous media bed also helps distribute the secondary burner exhaust flow more evenly. The diluted oxidizer stream persists about 100 mm downstream of the central jet exit plane, where surrounding air is entrained and is able to interact with the fuel jet as detailed in Figure 3.2. The resulting local increase in oxygen concentration produces a flame visibly different than the MILD reaction zone. The downstream location of this region provides a measure of the axial length of coflow influence. The extent of coflow influence is determined using this method, and was found to be consistent with the findings of [5]. The visibly apparent length of coflow influence is consistent with other studies performed using the JHC burner [5,6]. The outer surface of the coflow tube is well-insulated to reduce heat losses to the surroundings.

3.2 Vaporizer and Burner Control System

The burner requires an extensive control system to operate correctly and safely. The coflow reactants and primary fuel flows are each controlled separately. The flowrates of each of the four coflow inlet gasses (i.e. CH_4, H_2, N_2, and air) being fed into the secondary burner using calibrated orifice fittings. The pressure on the upstream and downstream side of each orifice were measured using pressure transducers (Prosense SPT25-10) calibrated using a high accuracy pressure measurement device (Omega PCL-1B) to an uncertainty of 0.69 kPa (0.1psi). The air and nitrogen orifices run in an unchoked configuration due to the higher flowrates used and the limited available source pressures. The methane and hydrogen ori-
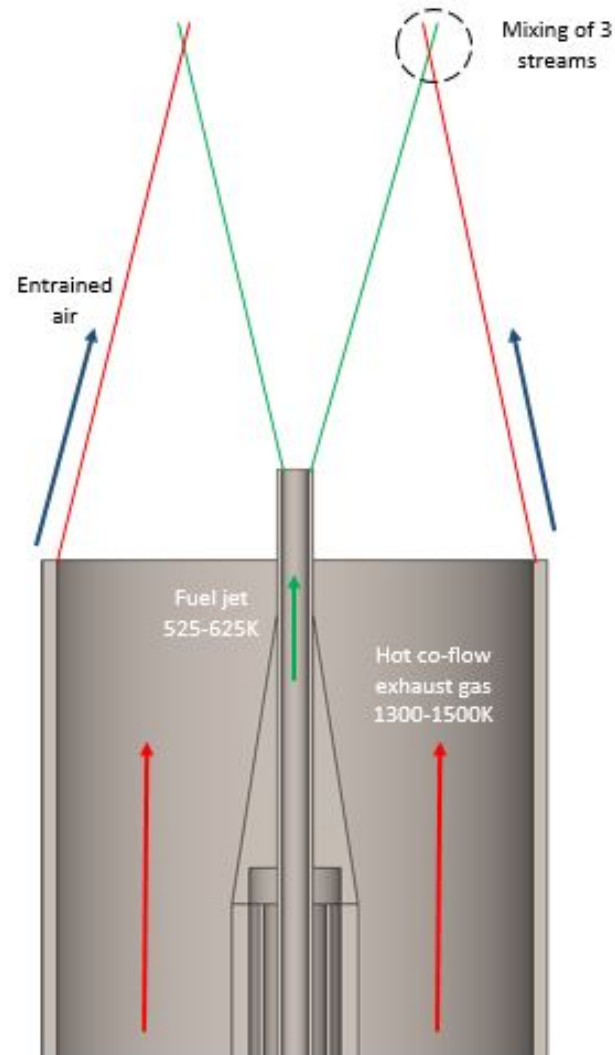
Figure 3.2: Illustration of interaction between primary fuel jet, coflow, and entrained air from the surroundings. The entrained air interacts with the fuel jet about 100 mm downstream.

fices run choked since the back pressure on the feed lines is much lower due to

the lower flowrates required. The methane and hydrogen orifices are calibrated

using a gilibrator. The calibration procedure is detailed in Appendix B and the uncertainties are reported in Table B.2.

The flowrate of each gas is controlled by adjusting the appropriate pressure regulator. The pressure measurements are converted into flowrates and read out using a LabVIEW program. The desired flowrates are input into the program and a red line denotes the required flowrate on continually updated plots. The regulators are adjusted so the measured flowrate matches the desired one, thereby making the white and red lines lie on top of each other. The temperature of the gas entering the orifice also significantly affects the measured flow rate. The nitrogen temperature can drop below freezing, as the expansion from a tank pressure of up to 17 Mpa [2500 psi] to a working pressure of less than 200 kPa [30 psi] lowers the temperature of the gas. The same expansion and cooling occurs with the methane and hydrogen, but both gasses run at much lower flowrates and pass through solenoid valves that output substantial heat when energized, causing the gasses to nominally be above room temperature. A K-type thermocouple is mounted just upstream of each orifice and must be closely monitored and the corresponding gas temperature adjusted in the Labview program to ensure accurate flowrates.

Four toggle switches operate solenoid valves that provide safety backups in the event of a power outage or emergency shutdown. Two normally closed valves provide shutoff for the methane and hydrogen streams. A normally open valve controls the nitrogen purge for the liquid fuel system. A three way valve controls the liquid fuel shunt system.

The second primary zone of the burner control system is the vaporizer and
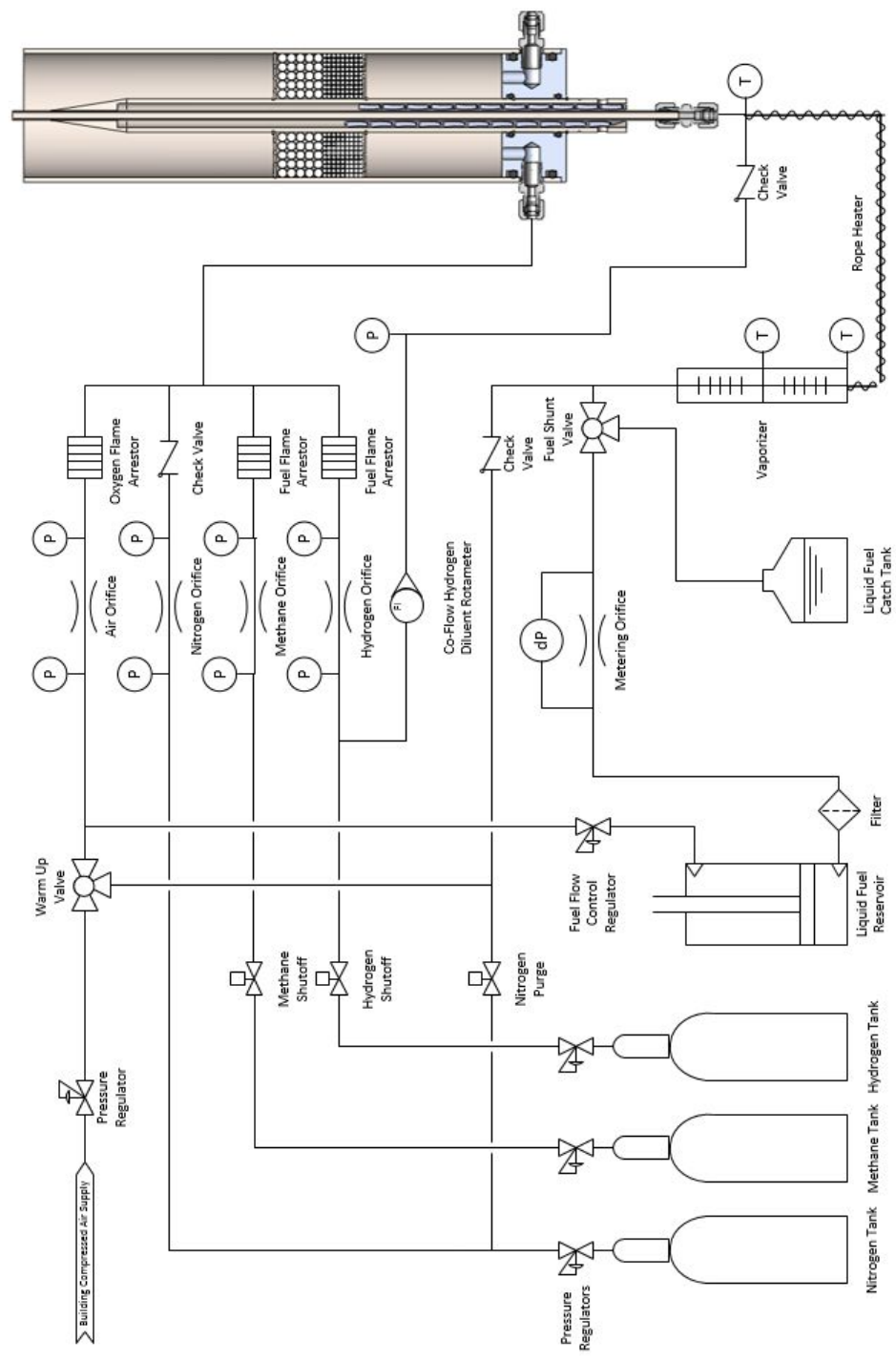
Figure 3.3: Plumbing and instrumentation diagram for both primary fuel jet and secondary burner control

primary fuel flow control. Liquid fuel is stored in a pneumatic cylinder with Buna-N seals and rated for 200psi. The flow rate of fuel is controlled by varying the pressure on the air side of the cylinder using the precision regulator (Omega PRG 200). The flow is metered using a swappable calibrated precision orifice (O'Keefe Controls IC-4006-09-SS or IC-4006-13-SS) and a differential pressure transducer (Validyne DP15-44) which has a range of 0-253 kPa [0-1900 torr]. The fuel system is primed by applying about 70kPa (10psig) of air pressure to the fuel cylinder, and then the fuel shunt switch is turned on to begin flowing fuel through the vaporizer.

The fuel is pressure-fed through an atomizing nozzle (Delevan 0.65 GPH, 60°A) at the vaporizer inlet. As fuel is first allowed to flow into the vaporizer, the spray pattern begins to develop, causing fluctuations in the orifice pressure drop reading. A steady flow rate is typically reached after about 10 seconds.

The vaporizer is adapted from a design provided by Sandia National Labs [45]. It consists of two six inch long, one inch diameter stainless steel tubes that are internally-finned to increase the surface area available for heat transfer. Heat is applied to the vaporizer using four 250 W, 120 VAC band heaters (Tempco NHW00106). The heaters are controlled in two zones by K-type thermocouples and solid state relay temperature controllers (MYPIN TD4-SNR+SSR). The first zone is typically set to 180°C and the second zone to 300°C under steady state operation. Two additional thermocouple/controller combinations are used to actively heat the fuel in the lines between the vaporizer and the burner. Both controllers are typically set to 300°C, but are occasionally adjusted (i.e. 250°C-350°C) to investigate the effect of varying the fuel jet temperature. The extra heaters prevent

the fuel from condensing due to heat loss to the ambient surroundings. The line heaters are also insulated to reduce heat losses.

The entire system is designed to default to a safe state in the event of power failure or emergency. If power is lost or the emergency stop button is pressed, all fuel flow is shut off with normally closed valves and the nitrogen purge is activated, purging any fuel currently in the vaporizer or coflow plumbing. All heaters are de-energized, and the nitrogen purge begins to cool down the system. The air supply also remains on, and assists with cooling the coflow. The liquid fuel tank remains pressurized since the air is still on, but the fuel flow is shunted into a local catch tank.

3.3   Experimental Conditions

3.3.1   Fuel Properties and Chemical Composition

Experiments were performed with three different large hydrocarbon fuels, referred to in this work as A2, C4, and C5. The naming convention is adopted from a multi-national research project funded by the FAA, where these same fuels have been used. A2 is the designator for Jet-A, a commonly-available aviation fuel. C4 and C5 are both experimental fuel blends. C4 is a 60/40 blend of Sasol IPK and Gevo ATJ, which are an iso-parrafinic kerosene (IPK) and an alcohol-to-jet fuel, respectively. C5 is a 73/27 blend of C10 isoparrafin and trimethylbenzene. These three fuels were chosen primarily to investigate the effect of their different chemistry

on turbulent flame liftoff in the MILD regime. A 2-D gas chromatography analysis of each fuel was provided by the Air Force Research Laboratory, which measured the weight percent of 83 different hydrocarbon compounds. These compounds were classified under four important categories of hydrocarbons, namely aromatics, iso-alkanes, n-alkanes, and cycloalkanes. The results of the analysis are shown in Figure 3.4. The commercial jet fuel A2 (Jet-A) is composed of all four of these compounds in a fairly even distribution. C4 is composed almost entirely of iso-alkanes, while C5 is composed of aromatics, iso-alkanes, and n-alkanes. C5 has a large aromatic content, which typically leads to increased soot production and radiation emission [46].

A2, C4, and C5 have some physical properties that are similar, but others are notably different. A number of important properties are presented in Table 3.1. The molecular weights of A2 and C4 are similar, while C5 has a significantly lower molar mass. The fuel jet exit velocity is affected by this difference, as the vaporized density of C5 is lower than that of A2 and C4. This produces a notably higher exit velocity (i.e. 8.3 m/s vs 6.4 m/s at Re = 10k) for the same mass flow rate. A higher jet velocity encourages higher entrainment rates, which enhances mixing. More mixing leads to decreased flame liftoff heights, as a flammable mixture of fuel and oxidizer is generated closer to the burner exit. The heat of combustion values of all three fuels are essentially the same. Also of note is the relatively low viscosity of C4. Lower viscosity requires less mass flow (which corresponds to heat release) to achieve a given Reynolds number, as seen in Equation 3.1.
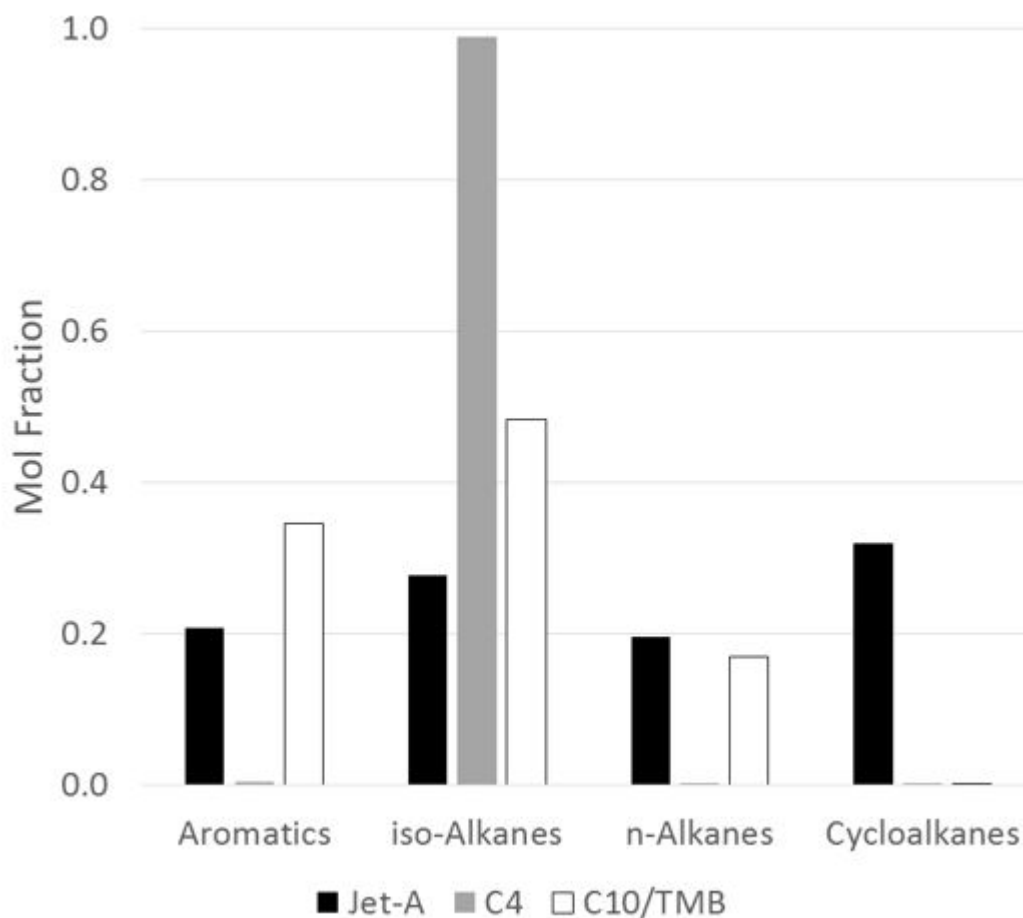
Figure 3.4: Comparison of major hydrocarbon categories contained in A2, C4, and C5

3.3.2 Primary Fuel Conditions

The primary fuel jet is controlled separately from the coflow, allowing independent variation of fuel parameters and coflow parameters. The fuel jet Reynolds number and exit temperature are varied according to the conditions noted in Table 3.2.

Table 3.1: Relevant properties of tested fuels

	A2	C4	C5
Average Molecular Weight (kg/kmol)	158.6	162.2	135.4
Density at 25°C (kg/m^3)	795.8	751.9	761.1
Heat of Combustion (MJ/kg)	43.06	43.81	43.01
Final Boiling Temperature (°C)	270.5	239.6	170.6
Viscosity at 250°C (kg/m-s)	N/A	9.282E-06	1.005E-05
Viscosity at 300°C (kg/m-s)	1.051E-05	1.011E-05	1.095E-05
Viscosity at 350°C (kg/m-s)	1.137E-05	1.092E-05	1.184E-05

The Reynolds number is defined as

$$Re = \frac{4\dot{m}}{\pi \mu D} \tag{3.1}$$

where $\dot{m}$ is the fuel mass flow rate, μ is the fuel viscosity at 300°C, and D is the fuel jet inner diameter. The fuel viscosity is determined using the correlation described in Appendix A at the desired exit temperature.

Widegren and Bruno [47] performed thermal decomposition measurements of Jet-A fuel in a jet-stirred reactor. At a temperature of 375°C, the amount of time required for 1% of the fuel to decompose was found to be at least 30 minutes. The fuel temperatures used in the current work are always less than 375°C, so less pyrolysis is expected to occur. The residence time of the fuel at elevated temperatures is expected to be on the order of 10^1s, which results in a conservative

Table 3.2: Primary fuel jet operating conditions for each fuel used. The effect of fuel jet exit temperature was investigated using C4 due to its low boiling point of 239°C, allowing data at 250°C to be collected.

| A2 | | | | | |
| Reynolds | Mass Flow Rate (g/s) | | | Jet Mean Exit Velocity (m/s) | | |
Number	250°C	300°C	350°C	250°C	300°C	350°C
3750		0.142			2.6	
5000		0.189			3.4	
6250		0.236			4.3	
7500		0.283			5.1	
8750		0.330			6.0	
10000		0.378			6.8	

| C4 | | | | | |
| Reynolds | Mass Flow Rate (g/s) | | | Jet Mean Exit Velocity (m/s) | | |
Number	250°C	300°C	350°C	250°C	300°C	350°C
3750	0.125	0.136	0.147	2.0	2.4	2.8
5000	0.167	0.182	0.196	2.7	3.2	3.8
6250	0.208	0.227	0.245	3.4	4.0	4.7
7500	0.250	0.272	0.294	4.0	4.8	5.7
8750	0.292	0.318	0.343	4.7	5.6	6.6
10000	0.333	0.363	0.392	5.4	6.4	7.5

| C5 | | | | | |
| Reynolds | Mass Flow Rate (g/s) | | | Jet Mean Exit Velocity (m/s) | | |
Number	250°C	300°C	350°C	250°C	300°C	350°C
3750		0.148			3.1	
5000		0.197			4.2	
6250		0.246			5.2	
7500		0.295			6.3	
8750		0.344			7.3	
10000		0.393			8.3	

estimation of 0.006% of the fuel undergoing pyrolysis. Therefore, it can be expected that negligible quantities of the large hydrocarbon fuels used in this study will undergo pyrolysis before being oxidized in the MILD environment.

3.3.3 Coflow Conditions

Setting and controlling the gas flow rates in the coflow is of vital importance to the collection of usable data from the burner. Setpoints have been determined to achieve a variety of coflow conditions, primarily varying the exhaust volumetric oxygen concentration and exit temperature. The flow rates and coflow conditions used during experimentation are presented in Table 3.3. The outlet compositions are shown in Table 3.4. The reported coflow oxygen concentration was determined using chemical equilibrium calculations with the reported flow rates. The reported coflow temperature was measured in a secondary experiment using a B-type thermocouple.

It is important to note that the inlet gas compositions were derived from equilibrium calculations to set the exit oxygen concentration and adiabatic flame temperature at the desired values. It was found that adiabatic flame temperatures (used in equilibrium calculations) of 1600K, 1800K, and 2000K produced measured exit temperatures of 1300K, 1400K, and 1500K respectively. The difference is due to heat loss through the burner walls. It was found that the measured exit temperatures would not vary by more than about 20K on a day-to-day basis. However, if the coflow insulation were to be significantly altered, the above relationship would

Table 3.3: Secondary Burner Inlet Flow Rates at Desired Outlet Conditions

Measured Temp [K]	O2 [vol %]	Air [LPM]	Nitrogen [LPM]	Methane [LPM]	Hydrogen [LPM]	Equivalence Ratio
1300	3	81.6	48.6	5.00	6.36	0.77
1400	3	79.1	33.5	5.00	6.36	0.79
1500	3	77.2	21.5	5.00	6.36	0.81
1300	6	101	31.7	5.00	6.36	0.62
1400	6	95.6	18.7	5.00	6.36	0.66
1300	9	120	14.6	5.00	6.36	0.52

no longer hold. It is not possible to operate above a coflow temperature of 1400K at an oxygen concentration of 9% or at 1500K and 6% O_2 because the secondary burner was found to not be stable at these conditions.

Table 3.4: Coflow Outlet Composition and Relevant Properties

Measured Temp [K]	O2 [vol %]	CO2 [vol %]	H2O [vol %]	N2 [vol %]	Velocity [m/s]	Density [kg/m^3]
1300	3	3	10	84	2.30	0.209
1400	3	3	10	84	2.26	0.185
1500	3	3	10	84	2.22	0.166
1300	6	3	10	81	2.34	0.210
1400	6	3	10	81	2.29	0.186
1300	9	3	10	78	2.37	0.211

The coflow exit temperature was measured using a B-type thermocouple (Omega

P30R-008) and a digital readout (Omega DPi8-EIT) at a number of radial locations approximately 10 mm above the coflow exit plane. The resulting measurements are corrected for radiation heat loss from the thermocouple bead using the method reported by Okhovat [48]. The experimental setup is shown in Figure 3.5.

The temperature distributions in the coflow (shown in Figure 3.6) were found to be within 20K of each other between R = 9 mm and R = 30 mm. The heat loss to ambient surroundings on the outer edge of the coflow is much greater than the heat lost to conduction along the central fuel tube, causing much lower coflow exit temperatures at larger radii.

Figure 3.5: Photograph of coflow temperature distribution measurement setup
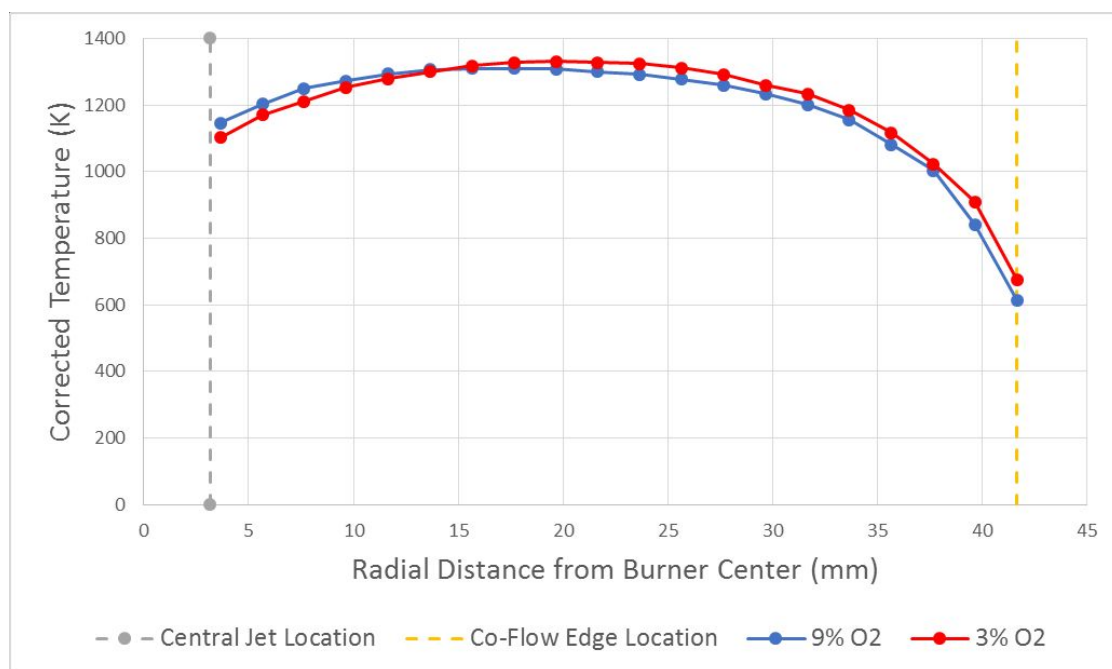
Figure 3.6: Temperature distribution in coflow for 3% and 9% oxygen concentration levels at an adiabatic flame temperature of 1300K

3.4   Data Collection and Processing

3.4.1   Visible Images

Visible images were acquired for some experimental conditions to allow qualitative comparison of the appearance of the MILD flames. The images were acquired using a Canon Rebel T-3 DSLR camera with a shutter speed of 2.5 s, an aperture of f/22, and an ISO of 100. The zoom setting of the camera could not be exactly matched for every condition, requiring post-processing of the images to ensure that they all contained the same field of view. The fuel jet tube was used as a fixed length reference to scale and crop the images to the desired size.

3.4.2   Chemiluminescence

Chemiluminescence is a chemically-excited emmission of light from a reaction. OH is an important radical in the combustion process, and emits relatively strong chemiluminescence in its excited state (referred to as OH*). Chemiluminescence measurements are performed using an Andor iStar 334t ICCD camera sensitive to light in the range of 230-1100 nm. A bandpass filter (Newport 10BPF10-310) with a center wavelength of 310 nm and a FHWM of 11 nm is used to isolate the OH* chemiluminescence from background radiation from the flame. The manufacturer-provided transmission spectrum is given in Figure 3.7.

The gate time is set to 5 ms and images are captured at 1.5Hz with a resolution of 700 x 280 pixels. The spatial resolution is typically 0.04 mm^2 per pixel. Two
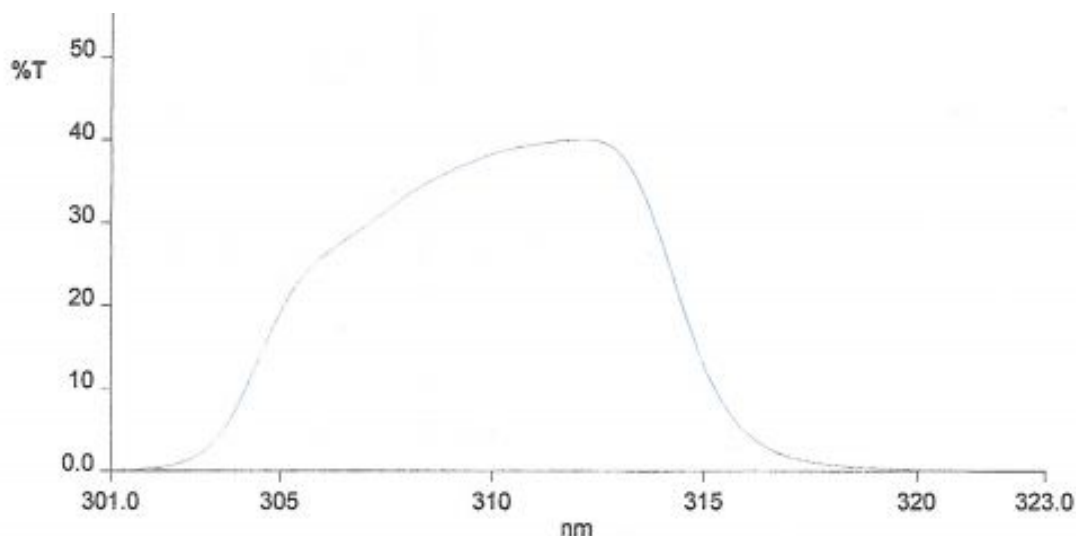
Figure 3.7: Transmission curve of 310 nm bandpass filter for both chemilumi-nescence and laser induced flourescence provided by the manufacturer (Newport Optics).

sets of images are acquired before the burner is lit. First, a series of 200 images is acquired without the 310 nm bandpass filter for spatial calibration. The fuel jet exit tube is used to determine both the spatial scale of the image (using the tube diameter) and location of the jet exit plane for liftoff height determination. Another series of 200 images is acquired with the filter on to collect data on the background radiation. The bandpass filter rejects almost all ambient light, so the average background intensity is normally below 500 photon counts per pixel with the above camera settings.

A series of 200 images is taken for each condition. Each image series is post-processed using a number of steps. First, a background subtraction is applied to

each image. The background subtraction reduces the interference of background noise and increases the signal-to-noise ratio of the image, especially when collecting images of flames with low OH* emission. Next, the images are averaged to provide a time-averaged OH* chemiluminescence map. A 2-D median filter is applied to the mean image to remove any local noise occurring due to dead pixels or image artifacts. Finally, the scaling determined using the spatial calibration is applied to the image and the location of the fuel jet exit plane is determined. The flame liftoff height is measured from the fuel jet exit plane.

The liftoff height is determined by a finding the point along the flame center line where the chemiluminescence signal intensity is equal to 10% of the difference between the maximum image intensity and the average background intensity. Determination of a single absolute liftoff height from a continuous intensity distribution is rather difficult. To account for the ambiguous nature of determining the true average flame liftoff height, a range of the expected liftoff location is presented. The range is defined by the location where the centerline intensity is equal to 7.5% and 12.5% of the difference described above, giving a 5% spread of intensity threshold where the flame liftoff height is expected to occur. The range is presented in the plots as solid bars on either side of the nominal liftoff height. Error bars extending outside this range represent the uncertainty in liftoff height determination.

3.4.3 Uncertainty

As discussed in Section 3.4.2, determining liftoff heights of these flames is ambiguous due to the lack of a definite transition in the OH* chemiluminescence intensity distribution. To account for the uncertain nature of measuring the liftoff height, a range of heights is presented along with the nominal height. In addition, there is some amount of bias and precision error associated with the measurement. It was found that the bias error originating from image noise was small compared to the precision error due to a large signal to noise ratio of at least 50. Precision error was not determined for each data point, as it would have required a prohibitively large number of tests. Instead, precision uncertainty was determined for a subset of cases that were expected to exhibit the largest variation in repeatability. These uncertainty values were then applied to all other data points as a conservative estimate of precision error. Liftoff height precision error was found to be approximately 1.2 mm, which was much larger than the maximum bias error of about 0.1 mm. Combined, these two sources of uncertainty result in a liftoff height error of about 1.3 mm, which is reflected by the error bars in the results.

It was found that uncertainty of the fuel jet Reynolds number is most sensitive to the uncertainty of the viscosity. In determining the viscosity uncertainty, it was found that the modeled mixture viscosity is most sensitive to the uncertainty in the methane reference viscosity. Methane is used as a reference fluid as discussed in Appendix A. The National Institute of Standards and Technology (NIST) specifies an uncertainty of 2% in methane viscosity at the desired conditions [49]. This

results in a typical mixture viscosity uncertainty of 2.1%. As a result, the uncertainty in Reynolds number is about 2%, and remains constant for all Reynolds numbers.

The fuel jet exit temperature was measured using a K-type thermocouple, which typically has an uncertainty of about 2.2K [50]. However, the measurement was performed approximately 200 mm from the actual exit of the jet. In the hot coflow (1300-1500K), it is expected that the actual exit temperature will increase as heat is transferred to the lower temperature fuel (525-625K). Thermocouple measurements of the jet exit temperature indicated that the actual exit temperature is only 1-2K greater than the thermocouple measurement 200 mm upstream. The reported fuel jet exit temperature uncertainty is therefore equal to about 2K.

Uncertainty in the coflow composition is presented in Appendix B. In summary, the average relative uncertainties in the air, nitrogen, methane, and hydrogen flowrates are 2.5%, 1.4%, 1.4%, and 1.5% respectively. Altogether, these uncertainties result in an absolute uncertainty in the calculated coflow equilibrium O_2 concentration of 0.8% by volume. Although this value is large compared to the oxygen concentrations reported to exist in the coflow, the reported oxygen concentrations of 3%, 6%, and 9% are sufficiently far apart to ensure that they can still be differentiated in a worst-case uncertainty stack up.

Uncertainty in the coflow temperature is significant, as this value was not measured in-situ. Instead, an auxiliary calibration experiment provided a detailed temperature map that was assumed to remain nearly constant from day-to-day. Even on the detailed temperature profile, the measured coflow exit temperature

was found to vary by about 200K when traversing the coflow. However, measurements on multiple days indicated that the temperature distribution remained reasonably uniform, with maximum temperature differences of about 20K in the same radial location. Increasing the uniformity of the coflow temperature distribution would be unrealistically difficult and is not expected to improve the quality of the data. The reported temperature values are taken as the maximum temperature in the coflow, which typically occurs at a radial distance from the burner center of approximately 15-20 mm. The uncertainty in the reported value is about 20K.

Chapter 4: Numerical Approach

In the study of flame liftoff, spatial distribution of dozens of species, local temperatures, and local fluid velocity are difficult or impossible to measure experimentally. Numerical simulations can provide insight into phenomena critical to flame liftoff such as ignition and detailed fluid-chemistry interaction that experiments cannot. Although it is very difficult to directly simulate a flame as complex as those stabilized on the JHC burner, simpler calculations can provide important clues to the mechanisms governing flame stability.

Calculations were performed using the Chemkin II chemical kinetics software [51]. Two subroutines in particular are employed: Senkin [52] and Oppdif [53]. A modified version of the pre-processing program TRANFIT was used to implement polynomial curve fits of binary diffusion coefficients to more accurately model transport properties [54]. Senkin simulates gas phase chemical kinetics in a closed homogeneous system, while Oppdif models an opposed flow laminar diffusion flame. A depiction of the opposed flame geometry shown in Figure 4.1 and is adapted from Lutz et al [1]. Separate fuel and oxidizer streams impinge on each other, creating a stagnation region where a flame can stabilize. The closed homogeneous reactor is a zero dimensional system and no geometry specifications are required. Calculation of the ignition delay time in a closed homogeneous reactor decouples the chemistry from species transport. Different fuel and oxidizer compositions can be studied

using ignition delay times to isolate the effect of chemistry on the liftoff behavior of JHC flames. An opposed flow diffusion flame provides a configuration that represents a real flame with transport properties and flame stretch, but can be simplified to a one dimensional analysis with reasonable accuracy.
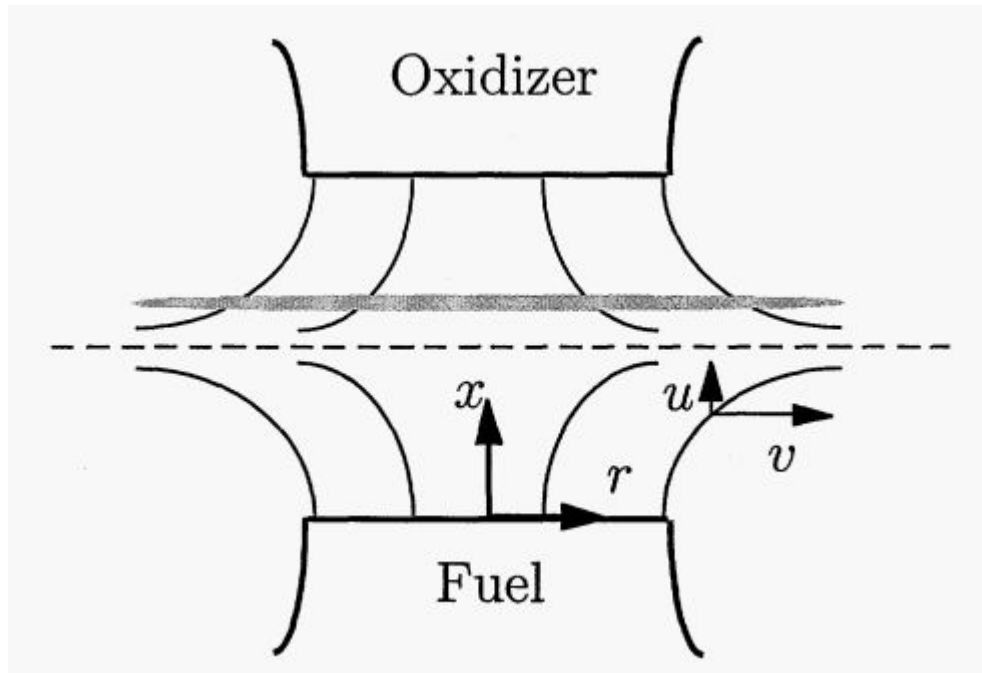
Figure 4.1: Geometry of the opposed flow diffusion flame. The dashed line represents the stagnation plane; the dotted region suggests the flame [1].

In order to model the combustion of the desired fuels, an appropriate chemical mechanism is required. To provide useful results, a mechanism must be validated for consistency over a range of parameters, such as laminar flame speed and ignition delay [15]. The mechanisms used for A2 and C5 fuels were designed specifically for those fuel blends by Dr. Hai Wang and his group at Stanford [55]. The C4 fuel

has no specific mechanism, so the mechanism for a fuel with a similar composition (Gevo ATJ, designated C1) is used. The main constituents of C1 are C_{12} isoalkane (78% by mass) and C_{16} isoalkane (16% by mass). The primary components of C4 are C_{10} isoalkane (15% by mass), C_{11} isoalkane (22% by mass) and C_{12} isoalkane (43% by mass). The carbon numbers of the main compounds in C4 are lower than those in C1, but the mass ratios of carbon to hydrogen atoms for the overall fuels are nearly identical (0.181 for C1 vs 0.182 for C4). Moreover, C1 is pure Gevo ATJ, and C4 contains 40% Gevo ATJ by volume along with additional iso-paraffinic compounds according to the GC x GC analysis from the AFRL. Although the chemical kinetics of C4 and C1 will differ, the composition data suggests that the trends will be comparable. At the time of writing, pure Gevo ATJ fuel (C1) was acquired to confirm the existence of similar flame liftoff height trends. Good agreement was found for all trends discussed in Section 5.

The reaction mechanisms were obtained via personal correspondence and have not been published in literature. However, publication is expected by September 2016 (at the time of writing) and experimental validation is being completed. The chemical mechanisms are nearly identical to the USC II C1-C4 mechanism developed by Wang et al. [56], with the exception of the inclusion of six thermal cracking reactions. Essentially, these six new reactions are added on to a pre-existing, well-validated mechanism.

4.1   Ignition Delay

Ignition delay calculations are used to isolate ignition chemistry from the effects of fluid mechanics such as strain and mixing. A zero-dimensional, constant pressure reactor is used to model the ignition of A2, C1, and C5 fuels at atmospheric pressure. An equivalence ratio of one is used for all simulations, and the initial mixture temperature is taken to be the coflow temperature. Ignition is expected to occur in a mixture with the highest reactivity, which typically occurs under fuel-lean conditions for the case of hot oxidizer and relatively cold fuel [57,58]. However, the ignition delay trends are found to be similar for stoichiometric conditions, which validates the use of an equivalence ratio equal to one [20].

A mixture of fuel, oxygen, nitrogen, carbon dioxide, and water vapor are used as initial species to simulate the conditions in the JHC burner. One mole of fuel is used, along with an oxidant mixture with the proportions as specified in Table 3.4. The required number of moles of each oxidizer species to achieve an equivalence ratio of one are used.

4.2   Laminar Opposed Flow Diffusion Flame

The goal of opposed flame calculations is to model the interaction of chemistry and fluid mechanics in a very simple configuration that is easily solved numerically but captures important physics present in more complex flames. Opposed flow flames have been used previously to study JHC burner flames [18–20,27] to decouple strain from the complex turbulent interactions that are observed experimentally [27]. To

apply opposed flow burner to MILD conditions, the oxidant stream is composed of products from the coflow exhaust, determined using chemical equilibrium. The compositions used in the calculations are detailed in Table 3.4. The desired coflow temperature is imposed upon the oxidizer stream to emulate the outlet conditions of the actual experiment. The fuel stream contains only the appropriate fuel at the desired temperature (typically 300°C). The velocities of each steam can be altered to achieve the desired average normal strain rate, which represents the average velocity gradient in the region where heat release is occurring. This value is used as the reported strain rate for all calculations.

Unless otherwise specified, the inlet velocities of fuel and oxidizer were imposed such that the average normal strain rate of the resultant flame was about 100 s^{-1}, a strain rate which has been found to provide good agreement to experimental data in JHC burner flames [22]. A mixture fraction coordinate is used to present the results of the simulation instead of a distance coordinate, which allows for visualization of species profiles across the reaction zone. The standard definition of mixture fraction based on the mass fraction of carbon and hydrogen atoms is not appropriate in combustion involving dilution of the oxidizer with CO_2 and H_2O due to the presence of C and H atoms in the oxidizer stream. A normalized mixture fraction, $\xi^* = (\xi - \xi_{ox})/(\xi_{fuel} - \xi_{ox})$, is used instead where ξ_{ox} and ξ_{fuel} refer to the standard definition of mixture fraction at the oxidizer and fuel stream boundaries. Using the mixture fraction, the results of opposed flame calculations can be visualized in the context of the experimental flames by traversing the reaction zone in the mixing region of the jet and coflow.

Chapter 5: Results and Discussion

The coflow oxygen concentration, coflow exit temperature, and primary fuel jet exit temperature were varied in order to investigate their role in the liftoff behavior of large hydrocarbon flames in a hot and diluted coflow. Experimental results are presented, observed trends in the data are noted, and explanations for the trends are given. Numerical results are provided to provide further insight into the experimental results.

5.1   Influence of Coflow Oxygen Concentration on Flame Liftoff

Liftoff heights were determined for A2, C4, and C5 flames from OH* chemilumines-cence images using the method described in Section 3.4.2. Results were obtained for flames in a coflow with a fixed exit temperature of 1300K, while the coflow oxygen concentration was varied between 3% and 9% by volume. The fuel jet Reynolds number was varied between 3,750 and 10,000. Visible images were also collected for a subset of the data (i.e. for Reynolds numbers 5000, 7500, and 10,000 only). It was found that flames in a coflow with 3% O_2 exhibited a spatial mis-match between where the flame was visible and where OH* chemiluminescence was observed. The mismatch is not observed in flames burning in a coflow with more oxygen available (i.e. 9%). Figure 5.1 shows a comparison between the cases of a

C5 flame in a coflow with 3% and 9% oxygen, respectively. Images of the other fuels exhibit similar characteristics and are omitted for brevity.
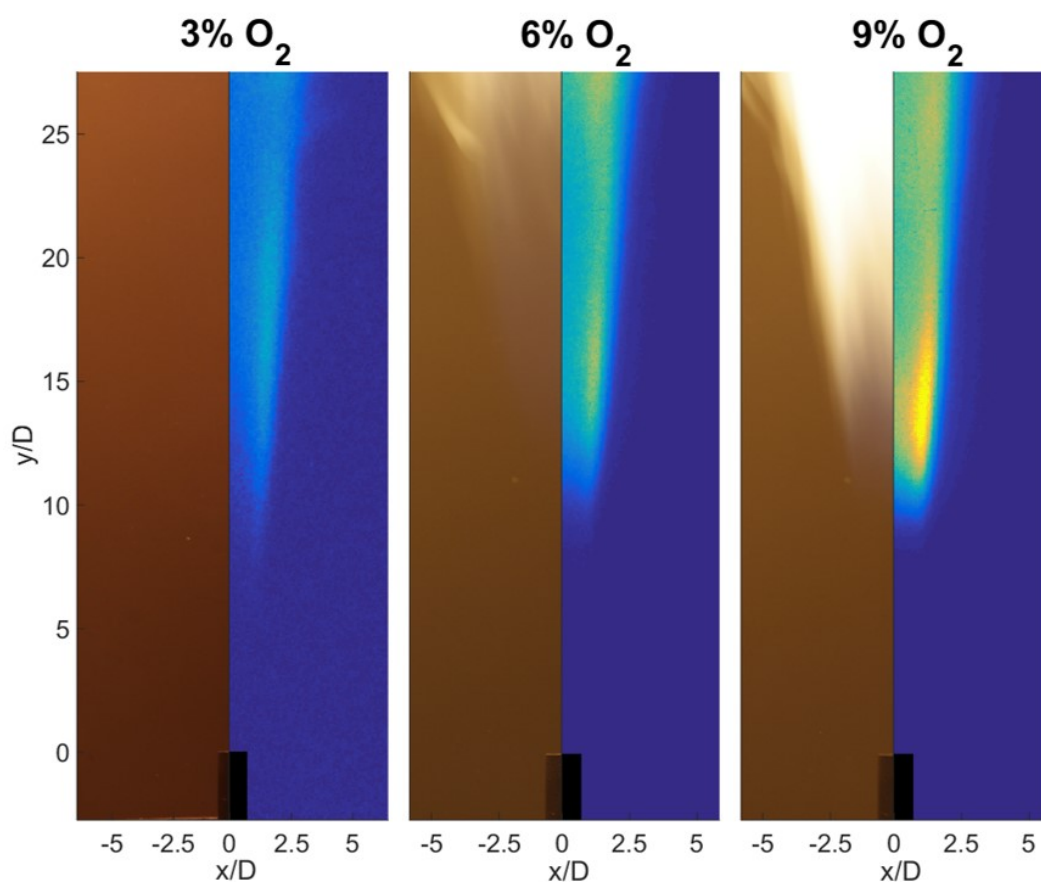
Figure 5.1: Comparison of visible images and OH* chemiluminescence images for a C5 flame burning in a coflow with an exit temperature of 1300K and volumetric oxygen concentrations of 3%, 6%, and 9%.

While the flame in a 3% O_2 coflow is not visible in the image, OH* chemi-luminescence indicates the presence of a reaction. In complete darkness, a very faint flame is visible in this region. A satisfactory image of this flame could not

be obtained. The presence of a nearly invisible flame in a hot coflow with a low oxygen concentration has been noted previously in MILD combustion of methane by Medwell et al [19,28]. Medwell attributed the cause of the low luminosity flame to the existence of a small temperature rise in the reaction zone. The temperature rise could not be discerned from the coflow temperature using Rayleigh scattering measurements, even though the presence of OH radicals confirmed that a reaction was indeed occurring [6]. These findings are consistent with the chemiluminescence and visible images of large hydrocarbon flames using the JHC burner. The need for chemiluminescence imaging to accurately measure flame liftoff heights in low oxygen conditions is underscored by these results.

The average liftoff heights measured using OH* chemiluminescence for flames in a coflow with an exit temperature of 1300K are presented in Figure 5.2. The instantaneous liftoff height in the chemiluminescene images appears to oscillate by up to 10 mm. A similar phenomenon has been observed previously [24, 40], and was attributed to continuous autoignition kernel formation and growth. The implications of this observation are discussed later.
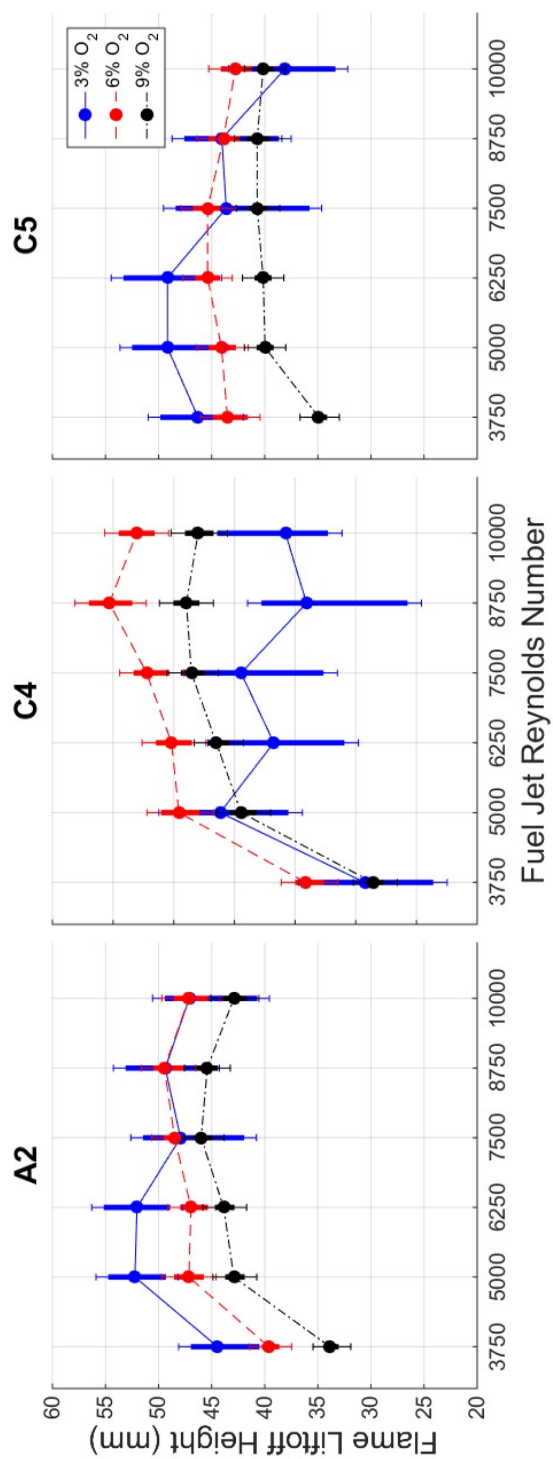
Figure 5.2: Measured flame liftoff heights for a fixed coflow temperature of 1300K. Coflow oxygen concentration and fuel jet Reynolds number are varied. The nominal liftoff heights are represented by the circular markers, the range of liftoff heights are denoted by the solid bars, and the uncertainties in the liftoff height range are represented by the error bars.

Three trends were noted in the flame liftoff height data. Each trend will be referred to in the following section as Trend 1, Trend 2, or Trend 3 according to the numeric designation below.

1. In coflows with 6% and 9% O_2, a difference in liftoff heights is observed between the three fuels. C4 produces flames with higher liftoff heights than A2 flames, while C5 flames have the lowest liftoff heights.

2. All fuels burning in coflow oxygen concentrations of 6% and 9% exhibit liftoff heights that first increase with fuel jet Reynolds number and then decrease slightly at Reynolds numbers greater than 7,500. The liftoff heights of flames in 6% O_2 are always higher than flames in 9% O_2.

3. Liftoff heights of flames in a coflow with 3% O_2 are found to decrease as the fuel jet Reynolds number is increased above 6,250. As a result, a non-monotonic trend in liftoff height as a function of coflow oxygen concentration was observed at fuel jet Reynolds numbers higher than 6,250. Liftoff heights first increase as the coflow oxygen concentration is increased from 3% to 6%, but they then decrease as it is changed from 6% to 9%. C4 flames exhibit a greater decrease in flame liftoff with increasing Reynolds number than either A2 or C5 flames.

The differences in flame liftoff heights between the three fuels noted in Trend 1 suggest a sensitivity to fuel chemistry. It has been noted previously that alkane structure influences ignition delay [59]. In order of increasing reactivity, aromatics, branched-chain alkanes, cycloalkanes, and straight-chain alkanes were studied.

However, the multi-component fuels under consideration in this work may not agree with this hierarchy, which is based on measurements for pure fuels. To investigate the relative reactivity of A2, C4, and C5, ignition delay calculations were performed. If fuel chemsitry is the dominant mechanism governing the liftoff height of flames in coflows with 6% and 9% O_2, C5 should have the shortest ignition delay times, followed by A2 and then C1 (representing C4 in this analysis). The results are presented in Figure 5.3 as a function of oxygen concentration.

C1 has the longest ignition delay times, followed by C5 and A2, respectively. Ignition delay times for C1 are approximately 3 times longer than A2 or C5 fuels at 6% and 9% oxygen concentrations. These results do not match the differences in liftoff heights noted in Trend 2, suggesting that fuel ignition chemistry is not the dominant mechanism in determining the liftoff heights of flames in coflow with an exit temperature of 1300K and oxygen concentrations of 6% and 9%.

Differences in the physical properties of the three fuels may explain the observed behavior. Although fuel jet Reynolds numbers are the same for each fuel, the jet exit velocities are notably different as shown in Figure 3.2. Jet velocity is directly related to entrainment [60], which is a process whereby fluid from the oxidizer stream is mixed with fluid from the fuel stream via large scale vortices caused by shear between the fuel jet and the coflow. A higher entrainment rate generally results in reduced ignition times due to better mixing between the fuel and oxidizer. Reduced ignition delay times result in lower liftoff heights.

The entrainment coefficient, which is the proportionality constant for the ratio of the mass flow rate of the jet to the mass of entrained fluid and the non-
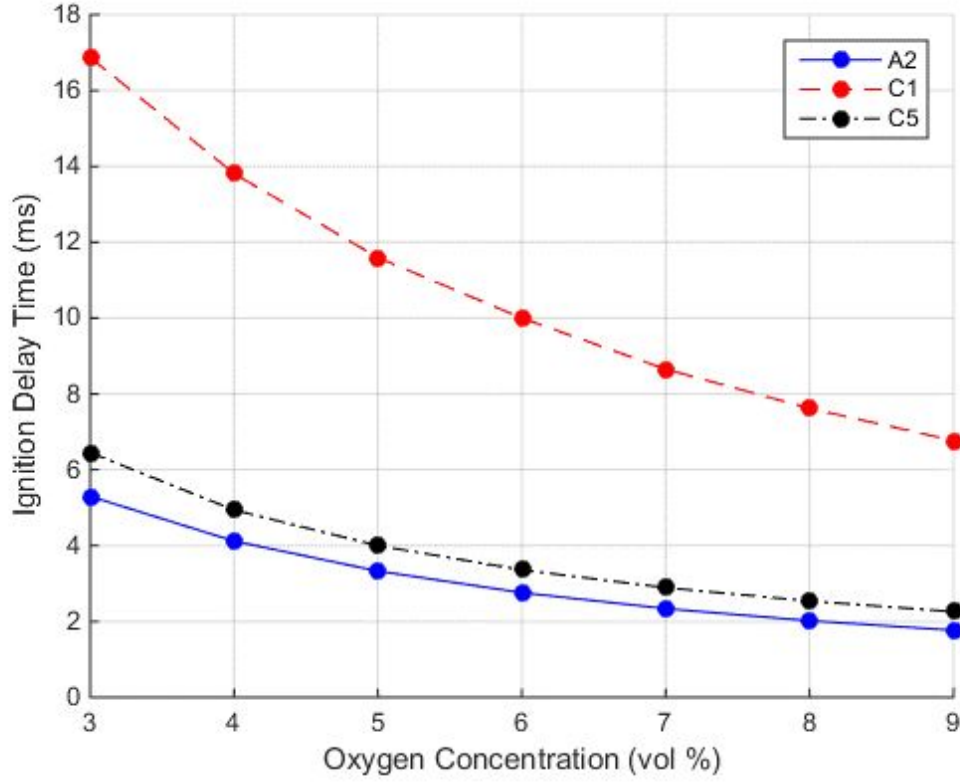
Figure 5.3: Comparison of ignition delay times for A2, C1, and C5 fuels over a range of 3% to 9% oxygen concentration at an initial mixture temperature of 1300K.

dimensional distance from the jet exit plane, was measured by Han et al [61] for a reacting jet in a coflow. Han developed a correlation for entrainment coefficient as a function of the density-weighted velocity ratio between the jet and coflow:

$$C = 0.13 \left(1 - e^{-0.036(r-1)}\right) \qquad r = \sqrt{\frac{\rho_{jet} u_{jet}^2}{\rho_{coflow} u_{coflow}^2}}, \qquad (5.1)$$

where u_{jet} is the fuel jet exit velocity, u_{coflow} is the coflow exit velocity, ρ_{fuel} is the fuel density at 300°C, and ρ_{coflow} is the coflow density at 1300K. This formulation is particularly relevant to the current experiments due to the large density difference between the fuel jet and the coflow. The entrainment coefficient represents the amount of coflow fluid entrained by the fuel jet, and thus provide a metric for the degree of mixing of the fuel and oxidizer streams.

Entrainment coefficients were calculated for relevant burner conditions and are presented in Table 5.1. The entrainment coefficients were not found to change significantly when the coflow oxygen concentration was varied and the coflow temperature remained at 1300K. The entrainment increased when the fuel jet velocity was increased, which was expected due to the larger momentum of the jet. The entrainment coefficients change with fuel type because the fuel densities are different, which produce different fuel jet exit velocities at equivalent Reynolds numbers. C5 had the largest entrainment coefficients (i.e. 16% higher than A2 or C4 fuels) owing to its lower vaporized density and therefore larger fuel jet exit velocity. The entrainment coefficients of A2 and C4 jets were within 4% of each other for equivalent Reynolds numbers. From these results, it would be expected that the liftoff heights of C5 flames would be lowest overall, with A2 flames having intermediate liftoff heights and C4 flames having the largest liftoff heights. The liftoff heights of C5 flames were about 10-20% lower than those of A2 or C4 flames for coflow oxygen concentrations of 6% and 9%. A2 flames were stabilized about 6% closer to the burner exit plane than C4 flames. The correlation of measured liftoff heights and calculated entrainment coefficients suggests that entrainment may play a role

in the stabilization of flames in coflows with 6% and 9% oxygen concentrations.

Table 5.1: Entrainment coefficients calculated for a constant coflow temperature of 1300K. The coflow oxygen concentration is varied, along with the fuel jet Reynolds number and fuel type.

A2			
Reynolds Number	Entrainment Coefficient (x100)		
	3% O2	6% O2	9% O2
3750	1.52	1.49	1.46
5000	2.12	2.08	2.04
6250	2.69	2.64	2.59
7500	3.22	3.17	3.12
8750	3.73	3.67	3.62
10000	4.22	4.15	4.09

C4			
Reynolds Number	Entrainment Coefficient (x100)		
	3% O2	6% O2	9% O2
3750	1.43	1.40	1.37
5000	2.01	1.97	1.93
6250	2.55	2.51	2.46
7500	3.07	3.02	2.97
8750	3.57	3.51	3.45
10000	4.03	3.97	3.91

C5			
Reynolds Number	Entrainment Coefficient (x100)		
	3% O2	6% O2	9% O2
3750	1.76	1.73	1.69
5000	2.42	2.38	2.33
6250	3.04	2.99	2.94
7500	3.63	3.57	3.51
8750	4.18	4.11	4.05
10000	4.69	4.63	4.56

The liftoff heights of flames in coflow with 6% O_2 are higher than those in

coflow with 9% O_2 for all Reynolds numbers and fuels as noted in Trend 2. This observation agrees with the premixing theory [38] (developed for non-MILD combustion) that flame liftoff height is inversely proportional to the flame speed [30]. The theory predicts that the flame liftoff height will occur where the local fluid velocity is equal to the flame speed, which increases with oxygen concentration [62].

Also noted in Trend 2 was a tendency of the flame liftoff height to initially increase with Reynolds number, but then decrease above a Reynolds number of approximately 7,500. Typical lifted, non-premixed jet flames (i.e. those not in MILD conditions) display liftoff heights that increase with the jet Reynolds number [29,30]. The behavior has been attributed to decreased fluid residence times caused by increased jet velocity, which causes ignition to occur further downstream. It is plausible that liftoff heights of flames at Reynolds numbers less than approximately 7,500 in coflows with 6% and 9% O_2 are governed by decreased fluid residence times, which causes ignition to occur further downstream. While the JHC flames exhibit behavior consistent with typical jet diffusion flames below Reynolds numbers of about 7,500, the decrease in liftoff height above this Reynolds number suggest the influence of a different mechanism.

A decrease in liftoff height with increasing Reynolds number has been observed previously in jet flames in hot and diluted coflows by Medwell et al. [6] and Oldenhof et al [24, 25]. Both studies suggested that an increase in entrainment and mixing could account for the unexpected behavior. Oldenhof was able to relate the decrease in liftoff height to the entrainment of hotter regions of coflow at earlier times, which causes a decrease in ignition delay and thus lower liftoff heights.

As seen in the coflow temperature profile in Figure 3.6, the peak temperature in the coflow occurs between the fuel jet and outer wall. An increase in entrainment caused by higher fuel velocities would cause this higher-temperature fluid to be mixed with unburned fuel at a lower axial distance, resulting in a decrease of flame liftoff heights consistent with the work of Oldenhof [25].

As noted in Trend 3, flames in a coflow with 3% O_2 were found to exhibit different trends than those in coflows with 6% and 9% O_2. A2 and C5 flames behave as expected (in accordance with the premixing theory [38]) for Reynolds numbers less than 6,250, as the liftoff height decreases monotonically with increasing oxygen concentration. At Reynolds numbers greater than 6,250, the liftoff height begins to drop below the liftoff heights of flames in coflows with higher O_2 concentrations. The behavior is even more pronounced in C4 flames, where the liftoff heights of flames in a coflow with 3% O_2 are always less than those found in flames with 6% O_2 and less than those in flames with 9% O_2 for Reynolds numbers greater than 5,000.

The non-monotonic trend observed in flame liftoff heights as a function of coflow oxygen concentration (above a fuel jet Reynolds number of 6,250) does not agree with the well-established premixing theory of [38], which suggests a monotonic decrease in flame liftoff height with increasing oxygen concentration. A very similar non-monotonic trend in flame liftoff was observed by Evans et al [21] when burning ethylene in the JHC burner. Evans attributed the behavior to a shift in the location of the most reactive mixture of fuel/oxidizer from regions of low scalar dissipation rate towards the high shear region of the jet, where scalar

dissipation is higher. The shift occurs due to a difference in stoichiometric mixture fraction, which increases as the oxygen concentration increases. An increase in the scalar dissipation rate delays ignition, causing flames in 6% O_2 to have larger liftoff heights than flames in 3% O_2. Flames in a coflow with 9% O_2 were found to have lower liftoff heights that flames in 6% O_2 due to the transition between MILD and autoignitive regimes, where ignition is more readily achieved at high scalar dissipation rates. It is plausible that the explanation of the non-monotonic trend in flame liftoff provided by Evans et al applies to the large hydrocarbon flames presented here. However, it does not explain why the liftoff heights of flames in 3% O_2 decrease to a greater degree than flames in 6% and 9% O_2 as the fuel jet Reynolds number is increased.

Flame liftoff heights are more strongly affected by the fuel jet Reynolds number in coflows with 3% O_2, indicating a sensitivity to either increased heat release or higher jet velocity at low oxygen levels. Both the heat release rate and jet velocity increase due to the larger mass flow rate of fuel required to achieve higher Reynolds numbers. Increased heat release has been shown to redirect flow streamlines and create low velocity regions that help stabilize lifted flames closer to the burner exit in accordance with the premixing theory [63]. The distribution of heat release under MILD conditions is expected to be locally less intense than normal combustion due to the presence of a distributed reaction zone [4, 64], which tends to have a lesser effect on streamline deflection. Furthermore, it has already been established that these flames do not obey the premixing theory, as indicated by the non-monotonic trend of flame liftoff height with increasing oxygen concentra-

tion. These findings suggest that heat release is not a dominant mechanism in the stabilization of large hydrocarbon JHC flames. Therefore, the dominant effect on the decrease in flame liftoff heights with increasing Reynolds number is attributed to the increased fuel jet velocity.

A higher excess velocity (difference between fuel jet and coflow velocities) causes two effects that should be considered separately: increased entrainment and increased strain of the flame front. Strain is the local deformation of fluid caused by viscous shearing forces and can affect chemical kinetics in the flame via increased molecular transport, which may enhance or weaken flame ignition and extinction phenomena. The role of entrainment in these flames was discussed along with Trend 2. Although entrainment coefficients are about 4% higher for jets in a coflow with 3% O_2, entrainment increases with Reynolds number at the same rate as in coflows with higher O_2 levels. Since entrainment is not expected to play a larger role in flames with 3% O_2, some other mechanism must control the liftoff height in these flames. Therefore, the decrease in flame liftoff height with increasing Reynolds number is most likely to be related to the increased strain caused by higher jet excess velocities.

Increased strain has been found to strongly enhance production of formaldehyde (CH_2O) in JHC flames, which is an important combustion precursor that can significantly decrease ignition delay times [20, 65]. It has been shown via CH_2O PLIF measurements that flames in a JHC burner generate significant quantities of formaldehyde on the fuel-rich side of the reaction zone [6, 22]. It is plausible that the formaldehyde is mixed into the incoming reactants via large shear-induced

turbulent structures or diffusion, where it reacts with the unburnt mixture and decreases the ignition delay time. A number of observations and previous research lend credibility to this explanation. Reaction zone weakening has been found to occur in methane and ethylene flames in diluted coflow with low oxygen concentrations (i.e. 3% by volume). The localized weakening allows fluid to penetrate the reaction zone more easily [27]. Convolution and weakening of the OH layer was found to occur more often at higher fuel jet Reynolds numbers [22], and suggests the presence of large scale recirculation structures. These structures can entrain the formaldehyde that penetrates the locally weakened reaction zone, transporting it into a low-velocity region. As fresh fuel/oxidizer mixture flows into the low-velocity region, it can interact with the formaldehyde and cause decreased ignition times.

Two computational analyses were performed to investigate whether or not the proposed phenomena can explain the observed liftoff height trends. Opposed flow flame calculations determine how oxygen concentration and strain affect formaldehyde formation in flames. Ignition delay calculations were then performed to elucidate how formaldehyde affects the ignition propensity for each fuel. The results of these two calculations can be combined to determine if the formaldehyde-induced reduction in ignition delay can account for the observed behavior.

As stated in Section 4.2, opposed flow laminar diffusion flame calculations are not strictly applicable to lifted flames in the region before ignition occurs. However, they do provide useful insight into the stabilization mechanisms of jet flames in a hot and diluted coflow. It should again be noted that no chemical

kinetic mechanism was available for C4 fuel. A mechanism for C1, which has comparable physical properties and a chemical composition similar to C4, was used instead. Results from opposed flow flame calculations are presented in Figure 5.4. Formaldehyde mole fraction is plotted against the normalized mixture fraction at two different average normal strain rates for A2, C1, and C5 flames with 3%, 6%, and 9% O_2 concentration in the oxidizer stream.

The maximum CH_2O concentration occurs well into the fuel-rich region of the flame for all fuels and strain rates for flames with 3% O_2, whereas the maximum CH_2O levels occur near the stoichiometric mixture fraction (as denoted by the triangular symbols) in the flames with 6% and 9% O_2. When the average normal strain rate is increased by a factor of five, the maximum mole fraction of CH_2O increases by a factor of 1-2 when the oxidant stream contains 6% or 9% O_2 and by a factor of 2-5 in 3% oxygen. These results are consistent with calculations performed for MILD methane flames by [20]. The maximum CH_2O mole fraction is 1.4-6 times higher for cases with 3% oxygen concentration than 6% or 9% cases at a strain rate of 100 s^{-1}. It is also noted that C1 has a maximum CH_2O concentration 1.7 times higher than A2 and 2.6 times higher than C5 in an oxidizer containing 3% O_2 at a strain rate of 100 s^{-1}.

Formaldehyde production is enhanced by both low oxygen concentrations and increased strain. The significantly higher CH_2O concentrations present in flames with 3% O_2 suggest that the proposed formaldehyde transport process will have a stronger effect in coflows with 3% O_2, especially considering that reaction zone weakening events occur more often at 3% O_2 levels [22]. When the O_2 concentration

56
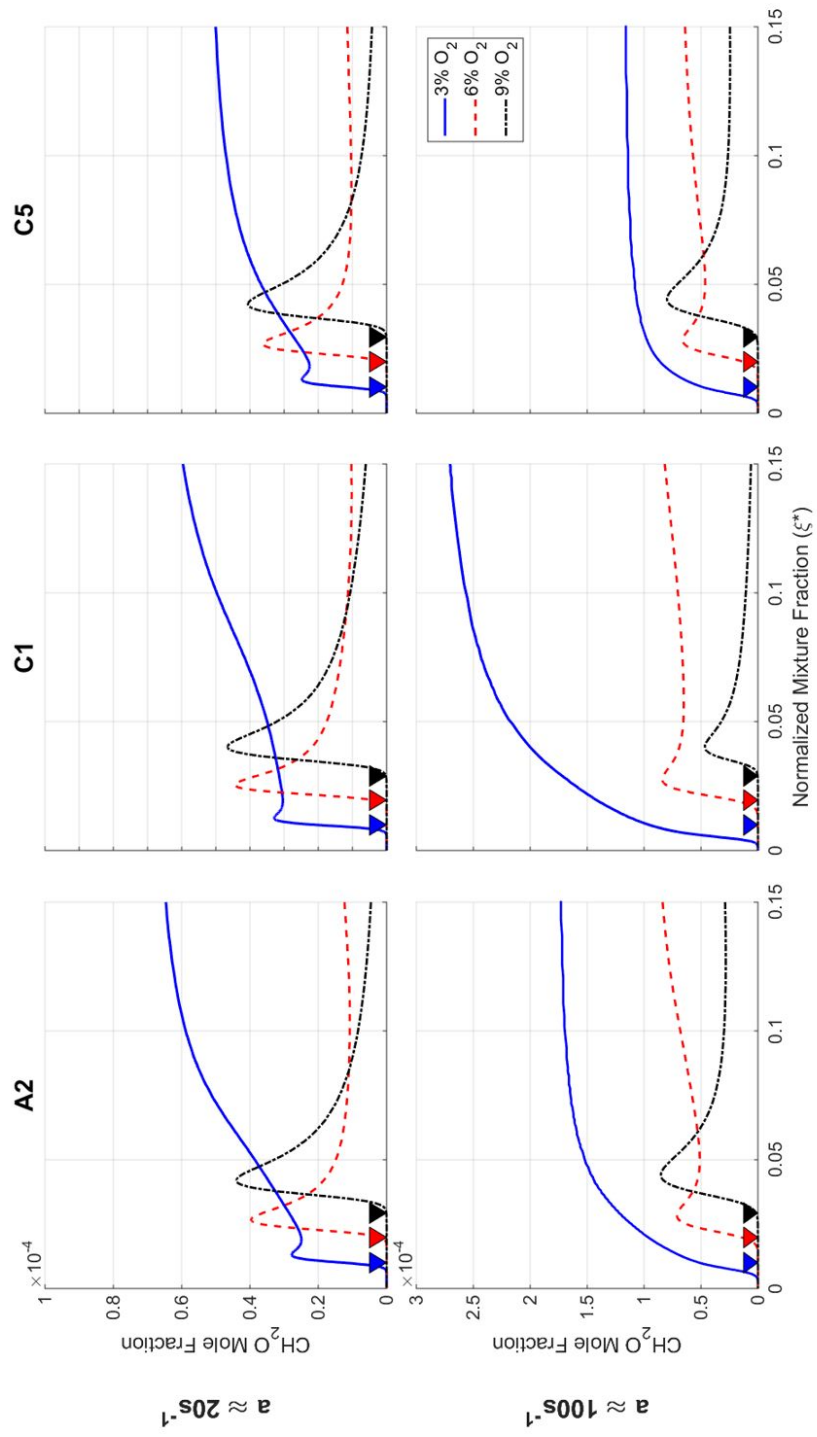
Figure 5.4: Formaldehyde mole fractions plotted as a function of normalized mixture fraction for oxidant stream O_2 levels of 3%, 6%, and 9% by volume. Note the different Y axis scales for the two different strain rates. The triangles denote the stoichiometric mixture fraction for each oxidant composition.

in the oxidizer stream is 3% by volume, formaldehyde concentrations are increased in the oxidizer-rich side of the stoichiometric mixture fraction, indicating that CH_2O penetration of the flame front is more likely.

The observed fuel sensitivity to the magnitude of Trend 3 may also explained by the numerical results. C1 has the highest mole fraction of formaldehyde of the three fuels, indicating that any transport of unconsumed CH_2O via the proposed process would produce a stronger effect on pre-ignition reactions than the other two fuels, provided that the frequency and strength of the entrainment remained the same. This observation is consistent with the measured flame liftoff heights, as C4 flames exhibit the most dramatic decrease in liftoff height with increasing fuel jet Reynolds number in the 3% O_2 case (relative to C4 flames in 6% and 9% O_2).

The addition of formaldehyde to an unburned mixture of fuel and oxidizer is found to substantially reduce ignition delay times in MILD conditions [20]. The normalized ignition delay times for A2, C1, and C5 are plotted against the added CH_2O mole fraction in Figure 5.5. A maximum initial CH_2O mole fraction of 1e-3 is shown, as the maximum mole fraction of CH_2O from the opposed flame calculations is on the order of 1e-4. It is expected that the concentration of CH_2O would not increase by more than an order of magnitude.

At these levels of formaldehyde concentration, it is expected that the ignition delay times for these large hydrocarbon fuels will reduce by 10-15%. Opposed flame calculations indicate that C4 flames produce the most formaldehyde, which reduces ignition delay more than in A2 or C5 flames (assuming transport of CH_2O to
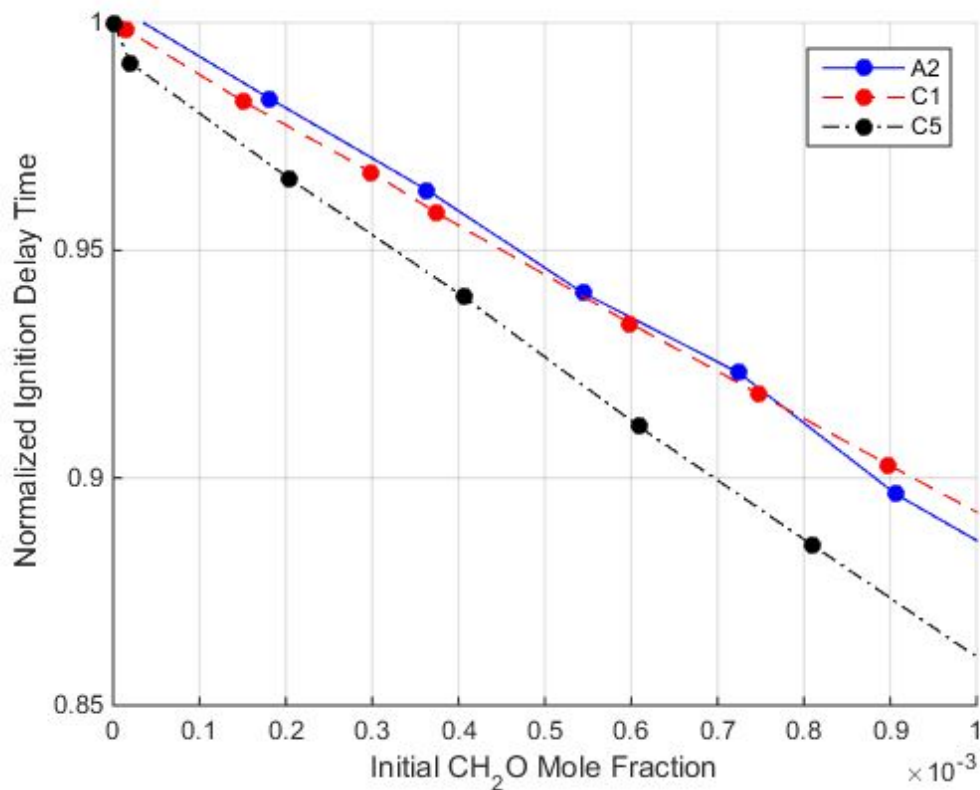
Figure 5.5: Normalized ignition delay times plotted against the initial CH_2O mole fraction. The values are normalized by the ignition delay time for a fuel/oxidizer mixture with no formaldehyde addition. The mixtures used in the calculations use $\Phi = 1$ and have initial oxygen concentrations of 3% by volume and initial temperatures of 1300K.

unburned regions is the same). C5 exhibits an increased sensitivity to formaldehyde addition, as ignition delay times are reduced by about 2.5% compared to A2 and C1 for the same mole fraction of formaldehyde addition. These results may account for the differences in flame liftoff heights (in 3% O_2) with fuel type. Although C5

produces less formaldehyde than A2, it has a higher ignition delay sensitivity to CH_2O addition. This may explain why the liftoff heights of C5 flames decrease more at larger Reynolds numbers than A2 flames.

5.2 Influence of Coflow Temperature on Flame Liftoff

It is of interest to determine how flame liftoff varies with coflow exit temperature. Liftoff heights were measured for A2, C4, and C5 flames in a coflow with a fixed oxygen concentration of 3% by volume, and coflow exit temperatures between 1300K and 1500K. The fuel jet Reynolds number was varied between 3,750 and 10,000. Visible images were collected at a fuel jet Reynolds number of 10,000 only. Visible images of flames at other Reynolds numbers were not acquired since their appearance did not change significantly with Reynolds number. An oxygen concentration of 3% was chosen due to its notable effect on the flame liftoff height as discussed in Section 5.1. A comparison of visible images and average OH* chemiluminescence images is presented in Figure 5.6.

As noted in Section 5.1, no flame is visible in the imaging region at a coflow exit temperature of 1300K. As the coflow temperature is increased, the visible region of the flame lowers into the field of view and the OH* chemiluminescence becomes more intense. The high luminosity region of the flame indicates an increase in the local oxygen concentration due to interaction with ambient air entrained into the coflow. The lowering of this region suggests an increase in entrainment of the coflow into the fuel jet, causing the local oxygen concentration to increase closer to the fuel jet exit plane. Formation of soot is increased in regions with higher oxygen concentration [66], which produces a high-luminosity flame seen in the images. This hypothesis is supported by calculation of the entrainment coefficients as described in Equation 5.1 for varying coflow temperatures, which show that entrainment rates
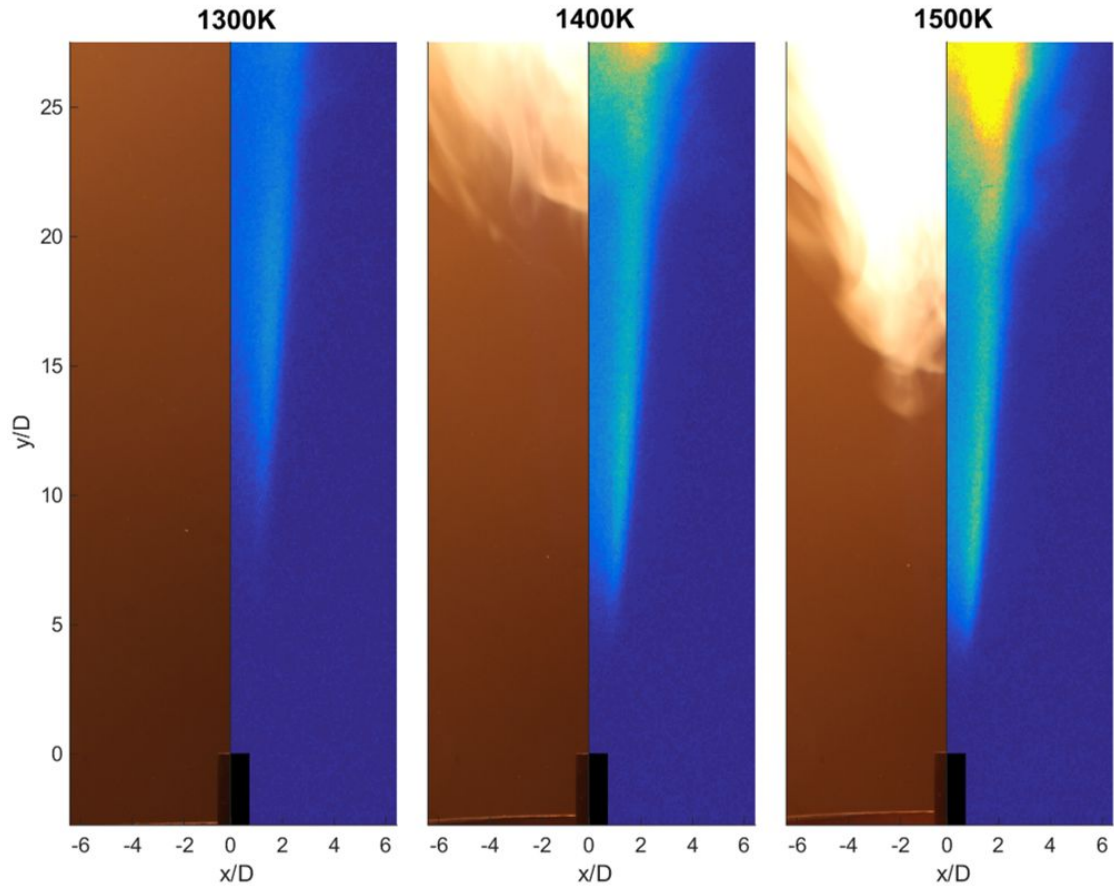
Figure 5.6: Comparison of long-exposure visible images (left) and OH* chemiluminescence images (right) for a C5 flame burning in a coflow with a volumetric oxygen concentration of 3% and measured exit temperatures of 1300K, 1400K, and 1500K. The scales of the chemiluminescence images are identical in this figure.

are increased by 13-20% when the coflow temperature is increased from 1300K to 1500K. The increase is primarily due to a decrease in the coflow density and a slight increase in the coflow velocity at higher temperatures. The entrainment coefficients are shown in Table 5.2.

Table 5.2: Entrainment coefficients calculated for a constant coflow oxygen concentration of 3% by volume. The coflow exit temperature is varied, along with the fuel jet Reynolds number and fuel type.

A2			
Reynolds	Entrainment Coefficient (x100)		
Number	1300K	1400K	1500K
3750	1.52	1.67	1.82
5000	2.12	2.31	2.49
6250	2.69	2.91	3.12
7500	3.22	3.48	3.72
8750	3.73	4.01	4.28
10000	4.22	4.52	4.80

C4			
Reynolds	Entrainment Coefficient (x100)		
Number	1300K	1400K	1500K
3750	1.43	1.58	1.72
5000	2.01	2.19	2.36
6250	2.55	2.77	2.98
7500	3.07	3.32	3.55
8750	3.57	3.84	4.10
10000	4.03	4.33	4.61

C5			
Reynolds	Entrainment Coefficient (x100)		
Number	1300K	1400K	1500K
3750	1.76	1.93	2.09
5000	2.42	2.63	2.83
6250	3.04	3.29	3.52
7500	3.63	3.90	4.16
8750	4.18	4.48	4.76
10000	4.69	5.02	5.32

The average liftoff heights measured using OH* chemiluminescence for flames in coflow with fixed oxygen concentration and varying temperature are presented in Figure 5.7. A monotonic decrease in flame liftoff height with increasing coflow temperature is observed. This trend is expected, as ignition delay time is approximately inversely proportional to initial temperature [67]. This causes the flame to ignite earlier, resulting in lower liftoff heights. This explanation is supported by ignition delay calculations in Table 5.3, which indicate that a temperature increase of 200K (with 3% O_2 by volume in the oxidant and $\Phi = 1$) results in a decrease in ignition delay of about 95% for all fuels considered.

Table 5.3: Ignition delay times as a function of initial mixture temperature for equivalence ratio equal to one and an oxygen concentration of 3% by volume.

Temperature [K]	Ignition Delay Time [ms]		
	A2	C1	C5
1300	5.3	16.9	6.5
1400	1.4	3.5	1.6
1500	0.42	0.87	0.46

The decrease in liftoff heights with increasing fuel jet Reynolds number observed in the 3% O_2 coflow at 1300K is seen to a lesser extent at coflow temperatures of 1400K and 1500K. Assuming that the sensitivity of flame liftoff height to the Reynolds number is caused by the strain and reaction zone weakening effects discussed previously, this observation suggests that CH_2O interaction with the unburned mixture becomes less prevalent at higher temperatures. Opposed flow laminar diffusion flame calculations (presented in Figure 5.8) support this conclu-
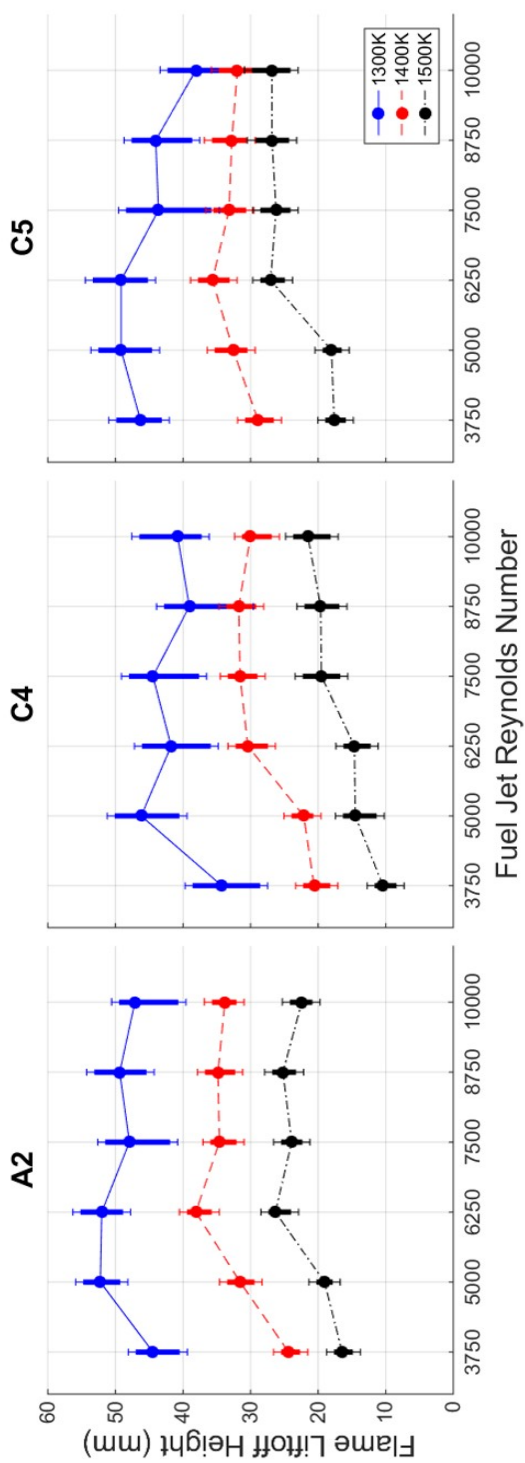
Figure 5.7: Measured flame liftoff heights for a fixed coflow oxygen concentration of 3% by volume. Coflow exit temperature, fuel jet Reynolds number, and primary fuel type are varied. The nominal liftoff heights are represented by the circular markers, the range of liftoff heights are denoted by the solid bars, and the uncertainties in the liftoff height range are represented by the error bars.

sion, as maximum formaldehyde mol fractions are reduced by 35-80% when the oxidizer stream temperature is 1500K compared to 1300K. With less formaldehyde available in the fuel-rich part of the flame, the effects of any transport through the reaction zone into unburnt mixture will be reduced.

Higher temperatures in the oxidizer stream promote a stronger reaction zone, as indicated by the 1.5 times higher intensity of OH* chemiluminescence at a coflow temperature of 1500K compared to 1300K. OH* has previously been used as an indicator of both the location and intensity of the reaction zone [68]. The effects of reduced ignition delay times and a strengthened reaction zone present at higher coflow temperatures appear to outweigh the influence of formaldehyde on the flame liftoff heights as the coflow temperature is increased. Flame stability is increased at higher coflow temperatures (as indicated by decreased liftoff heights) and the effects of fuel chemistry through formaldehyde production are diminished.
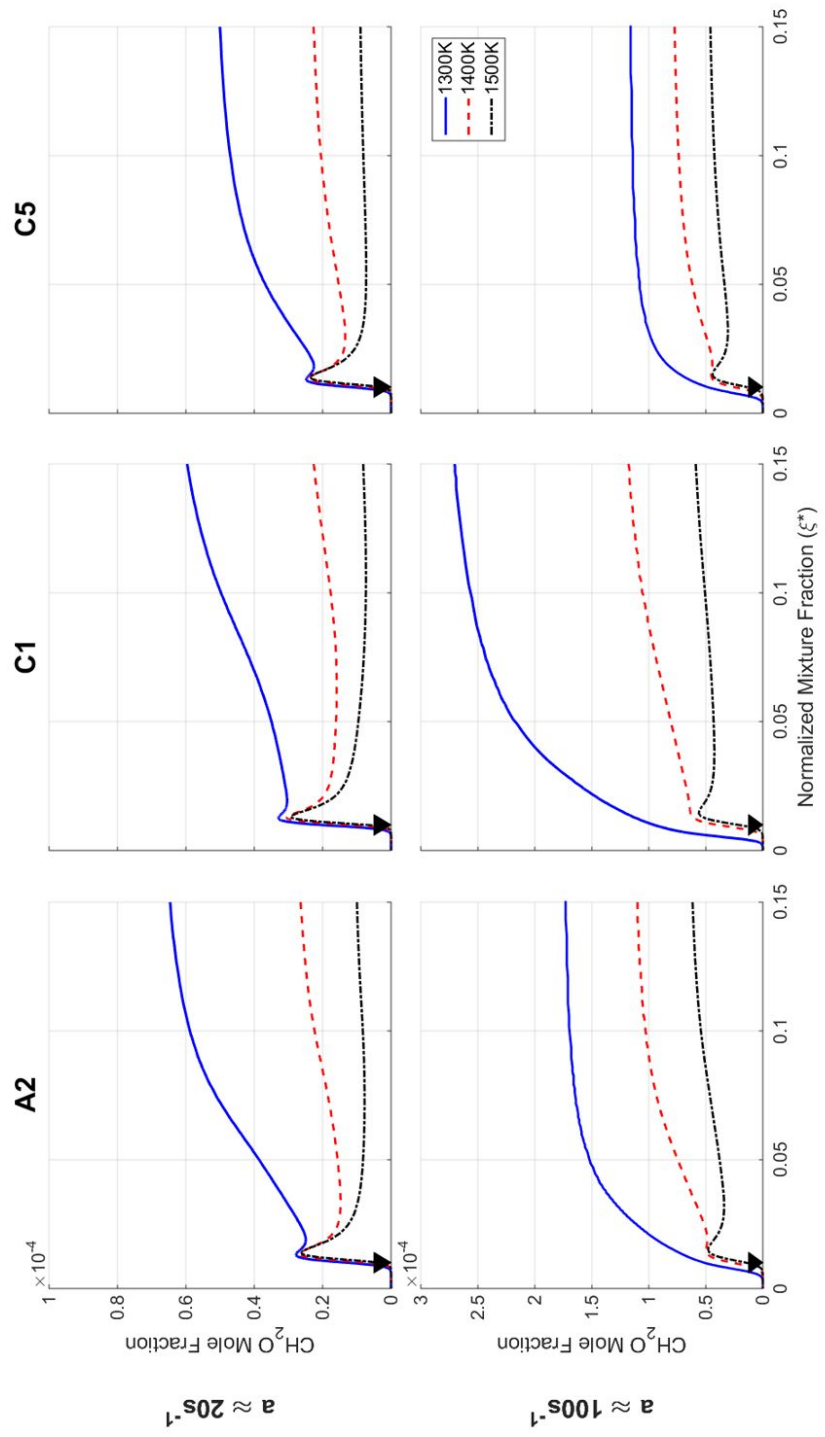
Figure 5.8: Formaldehyde mol fractions plotted as a function of normalized mixture fraction for oxidant stream temperatures of 1300K, 1400K, and 1500K at a fixed O_2 concentration of 3% by volume. Note the different Y axis scales for the two different strain rates. The triangles denote the stoichiometric mixture fraction, which only changes with fuel type.

5.3   Influence of Fuel Jet Temperature on Flame Liftoff

The outlet temperature of the primary fuel jet was varied to determine its effect on flame liftoff heights. Physically, this represents changing the fuel preheat temperature in practical devices. Only C4 fuel was tested due to limitations on achievable fuel flow rate and vaporizer heat output. Vaporized C4 has a low viscosity compared to A2 and C5, requiring a lower mass flow rate to achieve the desired Reynolds numbers than the other fuels. This property enables the vaporizer to provide sufficient heat to achieve a fuel jet exit temperature of 350°C at a Reynolds number of 10,000. C4 also has a relatively low boiling temperature of 240°C, which allows for testing at fuel jet temperatures meaningfully lower (250°C) than the typical 300°C. C5 has an even lower boiling point, but has the highest viscosity of the fuels that were tested, limiting the achievable operating conditions at higher temperatures due to the increase in viscosity with temperature. From the results obtained by varying the coflow temperature, it is expected that the three fuels that were tested will behave similarly under reduced/elevated fuel jet temperatures.

A coflow oxygen concentration of 9% by volume was used, as it produces the most luminous flames. The increased luminosity resulted in decreased uncertainty in the liftoff location, which enhances the clarity of the liftoff height trends. The coflow exit temperature was fixed at 1300K. The results for a fuel jet temperatures of 250°C, 300°C, and 350°C are presented in Figure 5.9.

Flame liftoff heights were found to decrease as the fuel jet temperature was
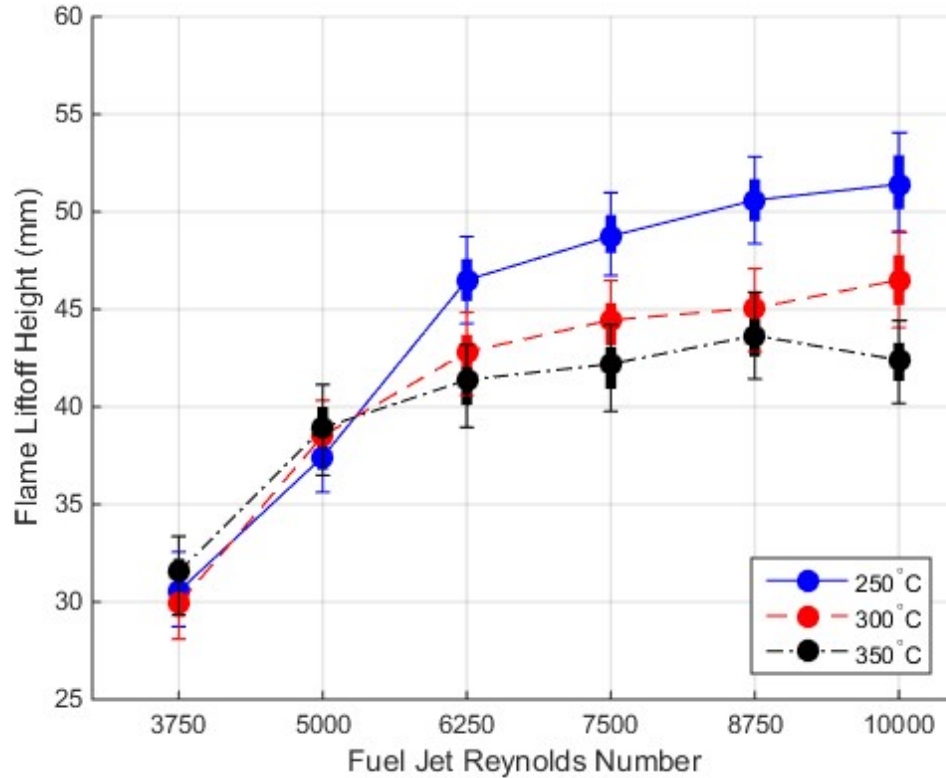
Figure 5.9: Measured flame liftoff heights for a fixed coflow oxygen concentration of 9% by volume and a fixed coflow temperature of 1300K. The exit temperature of the fuel jet is varied. The nominal liftoff heights are represented by the circular markers, the range of liftoff heights are denoted by the solid bars, and the uncertainties in the liftoff height range are represented by the error bars.

increased, but only when the Reynolds number was greater than or equal to 6250. At Reynolds numbers below 6250, the flame liftoff heights are essentially indistinguishable as the bounds of uncertainty overlap. Entrainment coefficient calculations (shown in Table 5.4) indicate that entrainment is increased by about 50% by

increasing the fuel jet temperature from 250°C to 350°C at a Reynolds number of 3750, but only by 35% at a Reynolds number of 10,000. Therefore, it appears that entrainment does not significantly affect the location of the flame liftoff height at low Reynolds numbers (where entrainment most strongly increases with fuel jet temperature), but may have a stronger influence at higher Reynolds numbers.

Table 5.4: Entrainment coefficients as a function of fuel jet temperature and Reynolds number for C4 fuel.

C4			
Reynolds	Entrainment Coefficient (x100)		
Number	250°C	300°C	350°C
3750	1.09	1.37	1.67
5000	1.57	1.93	2.31
6250	2.03	2.46	2.91
7500	2.48	2.97	3.47
8750	2.90	3.45	4.01
10000	3.31	3.91	4.51

Ignition delay times are expected to be shorter for higher fuel jet temperatures, as higher mixture temperatures produced shorter ignition times in calculations that were discussed in Section 5.1. Due to the nature of the perfectly mixed, zero dimensional model, the temperatures of fuel and oxidizer cannot be varied independently. To assess the impact of the change in fuel temperature on the overall mixture temperature, a mass-weighted mixture temperature will be used. The mass-weighted mixture temperature is formulated as

$$T_{avg} = T_{fuel}\frac{m_{fuel}}{m_{fuel} + m_{ox}} + T_{ox}\frac{m_{ox}}{m_{fuel} + m_{ox}}, \tag{5.2}$$

where T_{fuel} and T_{ox} are the fuel and oxidizer stream temperatures and m_{fuel} and m_{ox} are the mass of fuel and oxidizer present in the closed homogeneous reactor. The average mixture temperature increases by only 1K for a 100K change in the fuel temperature. It is not expected that this change in the average mixture temperature will cause any noticeable variation of flame liftoff height due to decreased ignition delay time. It can therefore be concluded that a decrease in ignition delay time due to an increase in the fuel jet temperature is not responsible for the decreased liftoff heights observed at higher Reynolds numbers.

It is plausible that the increase in entrainment noted earlier begins to have a more significant effect at higher Reynolds numbers (i.e. $> 5,000$) in a coflow with 9% O_2 concentration. An increase in turbulence is known to cause an increase in entrainment [69]. Transition to fully turbulent flow in a pipe typically occurs at a Reynolds number of about 4,000 [70]. Developed turbulent flow is characterized by steeper velocity gradients near the pipe wall compared to laminar flow, where the velocity profile is parabolic. It is possible that higher velocity gradients near the jet-coflow boundary promote better mixing between the fuel and oxidizer streams. Faster mixing results in decreased ignition delay times.

Velocity gradients near the tube wall are increased when the mean jet exit velocity is increased. An increase in the fuel jet temperature results in higher mean jet exit velocities, as the increase in fuel viscosity with temperature requires a larger

mass flow rate to achieve the same Reynolds number. The increase in jet velocity outweighs the effect of the decrease in the fuel density as the temperature is raised, which would tend to lower entrainment rates.The transition to a fully turbulent velocity profile at the jet exit coupled with increased entrainment at higher fuel temperatures may explain the change in liftoff behavior around a Reynolds number of 5,000.

Chapter 6: Summary and Conclusions

In summary, mechanisms governing the liftoff heights of large hydrocarbon flames under MILD-like conditions were investigated. The work was motivated by a need to understand the stabilization phenomena of large hydrocarbon fuels in MILD conditions for effective implementation in practical devices such as industrial furnaces and gas turbine engine combustors. A laboratory-scale burner with a central fuel jet in an annular hot and diluted coflow was used to emulate MILD combustion conditions in a non-premixed configuration. The coflow was designed to produce low oxidizer concentrations at elevated temperatures, which is required to achieve MILD combustion. Coflow exit conditions were varied to assess the impact of oxygen concentration and reactant temperature on the stabilization of lifted flames in the MILD regime. The fuel jet exit temperature was varied to determine how the fuel temperature affects flame liftoff compared to the oxidant temperature. Opposed flow laminar diffusion flame calculations were performed to investigate the effect of oxygen concentration and temperature on fuel chemistry. Strain-induced formaldehyde concentration changes were noted. Ignition delay calculations were performed to determine the effect of minor species on flame liftoff through a change in the ignition chemistry.

The conclusions from this effort are as follows:

I Fuels with low density and high viscosity produced flames with lower liftoff heights, which was attributed to increased entrainment resulting from the higher jet exit velocity. These entrainment effects outweighed differences in fuel-dependent ignition chemistry for flames in coflows with 6% and 9% O_2.

II Liftoff heights of flames in coflows with 6% and 9% O_2 initially increased with Reynolds number, but then began to decrease above a Reynolds number of 7,500. The behavior was attributed to a decrease in ignition chemistry timescales caused by entrainment and turbulent mixing that begins to outweigh the effect of increased jet momentum at a Reynolds number of 7,500.

III Increasing the fuel jet Reynolds number when the coflow contains 3% O_2 and has an exit temperature of 1300K causes a reduction in flame liftoff heights. This behavior was determined to be related to formaldehyde transport through the reaction zone and subsequent entrainment into regions of unburned fluid, resulting decreased in ignition delay times. The reduced ignition times reduce flame liftoff heights.

IV Increasing the coflow temperature causes flames in 3% O_2 to become less sensitive to formaldehyde. This is evidenced by the lack of a reduction in liftoff heights with increased Reynolds numbers that was observed in a 1300K

coflow. Evidence is also seen in opposed flame calculations, where an increase in the oxidant stream temperature causes a reduction in CH_2O concentrations.

Bibliography

[1] A. Lutz, R. Kee, J. Grcar, and F. Rupley, "OPPDIF: A Fortran program for computing opposed-flow diffusion flames," Tech. Rep. May, 1997.

[2] H. Tsuji, A. K. Gupta, T. Hasegawa, M. Katsuki, K. Kishimoto, and M. Morita, *High Temperature Air Combustion.* CRC Press, 2002.

[3] G. SZEGO, B. DALLY, and G. NATHAN, "Scaling of NOx emissions from a laboratory-scale mild combustion furnace," *Combustion and Flame*, vol. 154, pp. 281–295, July 2008.

[4] A. Cavaliere and M. de Joannon, "Mild Combustion," *Progress in Energy and Combustion Science*, vol. 30, pp. 329–366, Jan. 2004.

[5] P. R. Medwell, "Laser diagnostics in MILD combustion," *School of Mechanical Engineering*, 2007.

[6] P. R. Medwell, P. a. M. Kalt, and B. B. Dally, "The role of hydrogen addition on the structure and stability of hydrocarbon flames in a JHC burner," *7th High Temperature Air Combustion and Gasification International Symposium*, no. January, pp. 2–6, 2008.

[7] C. GALLETTI, A. PARENTE, and L. TOGNOTTI, "Numerical and experimental investigation of a mild combustion burner," *Combustion and Flame*, vol. 151, pp. 649–664, Dec. 2007.

[8] A. F. Colorado, B. A. Herrera, and A. A. Amell, "Performance of a flameless combustion furnace using biogas and natural gas.," *Bioresource technology*, vol. 101, pp. 2443–9, Apr. 2010.

[9] B. Danon, E.-S. Cho, W. de Jong, and D. Roekaerts, "Numerical investigation of burner positioning effects in a multi-burner flameless combustion furnace," *Applied Thermal Engineering*, vol. 31, pp. 3885–3896, Dec. 2011.

[10] V. K. Arghode and A. K. Gupta, "Effect of flow field for colorless distributed combustion (CDC) for gas turbine combustion," *Applied Energy*, vol. 87, pp. 1631–1640, May 2010.

[11] V. K. Arghode, A. E. Khalil, and A. K. Gupta, "Fuel dilution and liquid fuel operational effects on ultra-high thermal intensity distributed combustor," *Applied Energy*, vol. 95, pp. 132–138, July 2012.

[12] V. Mahendra Reddy, D. Sawant, D. Trivedi, and S. Kumar, "Studies on a liquid fuel based two stage flameless combustor," *Proceedings of the Combustion Institute*, vol. 34, pp. 3319–3326, Jan. 2013.

[13] S. Kruse, B. Kerschgens, L. Berger, E. Varea, and H. Pitsch, "Experimental and numerical study of MILD combustion for gas turbine applications," *Applied Energy*, vol. 148, pp. 456–465, 2015.

[14] M. Derudi and R. Rota, "Experimental study of the mild combustion of liquid hydrocarbons," *Proceedings of the Combustion Institute*, vol. 33, pp. 3325–3332, Jan. 2011.

[15] C. K. Westbrook, W. J. Pitz, O. Herbinet, H. J. Curran, and E. J. Silke, "A comprehensive detailed chemical kinetic reaction mechanism for combustion of n-alkane hydrocarbons from n-octane to n-hexadecane," *Combustion and Flame*, vol. 156, no. 1, pp. 181–199, 2009.

[16] J. Ye, P. R. Medwell, E. Varea, S. Kruse, B. B. Dally, and H. G. Pitsch, "An experimental study on MILD combustion of prevaporised liquid fuels," *Applied Energy*, vol. 151, pp. 93–101, Aug. 2015.

[17] M. De Joannon, A. Cavaliere, R. Donnarumma, and R. Ragucci, "Dependence of autoignition delay on oxygen concentration in mild combustion of high molecular weight paraffin," *Proceedings of the Combustion Institute*, vol. 29, pp. 1139–1146, Jan. 2002.

[18] B. Dally, A. Karpetis, and R. Barlow, "Structure of turbulent non-premixed jet flames in a diluted hot coflow," *Proceedings of the Combustion Institute*, vol. 29, pp. 1147–1154, Jan. 2002.

[19] P. R. Medwell and B. B. Dally, "Effect of fuel composition on jet flames in a heated and diluted oxidant stream," *Combustion and Flame*, vol. 159, pp. 3138–3145, Oct. 2012.

[20] P. R. Medwell, D. L. Blunck, and B. B. Dally, "The role of precursors on the stabilisation of jet flames issuing into a hot environment," *Combustion and Flame*, vol. 161, no. 2, pp. 465–474, 2014.

[21] M. Evans, P. Medwell, H. Wu, A. Stagni, and M. Ihme, "Classification and lift-off height prediction of non-premixed MILD and autoignitive flames," *Proceedings of the Combustion Institute*, 2016.

[22] P. R. Medwell, P. A. Kalt, and B. B. Dally, "Simultaneous imaging of OH, formaldehyde, and temperature of turbulent nonpremixed jet flames in a heated and diluted coflow," *Combustion and Flame*, vol. 148, pp. 48–61, Jan. 2007.

[23] P. R. Medwell and B. B. Dally, "Experimental observation of lifted flames in a heated and diluted coflow," *Energy and Fuels*, vol. 26, no. 9, pp. 5519–5527, 2012.

[24] E. Oldenhof, M. Tummers, E. van Veen, and D. Roekaerts, "Ignition kernel formation and lift-off behaviour of jet-in-hot-coflow flames," *Combustion and Flame*, vol. 157, pp. 1167–1178, June 2010.

[25] E. Oldenhof, M. Tummers, E. van Veen, and D. Roekaerts, "Role of entrainment in the stabilisation of jet-in-hot-coflow flames," *Combustion and Flame*, vol. 158, pp. 1553–1563, Aug. 2011.

[26] J. E. Dec and E. B. Coy, "OH Radical Imaging in a DI Diesel Engine and the Structure of the Early Diffusion Flame," in *SAE Technical Paper*, SAE International, 1996.

[27] P. R. Medwell, P. a. M. Kalt, and B. B. Dally, "Reaction Zone Weakening Effects under Hot and Diluted Oxidant Stream Conditions," *Combustion Science and Technology*, vol. 181, no. 7, pp. 937–953, 2009.

[28] P. R. Medwell, P. a. M. Kalt, and B. B. Dally, "Imaging of diluted turbulent ethylene flames stabilized on a Jet in Hot Coflow (JHC) burner," *Combustion and Flame*, vol. 152, no. 1-2, pp. 100–113, 2008.

[29] G. T., "Lift-off Heights and Visible Lengths of Vertical Turbulent Jet Diffusion Flames in Still Air," *Combustion Science and Technology*, vol. 41, no. 1-2, pp. 17–29, 1984.

[30] S. R. Turns, *An Introduction to Combustion Concepts and Applications*. New York: McGraw-Hill, 2012.

[31] M. D. Durbin, M. D. Vangsness, and D. R. Ballal, "Study of Flame Stability in a Step Swirl Combustor," in *ASME 1995 International Gas Turbine and Aeroengine Congress and Exposition*, 1995.

[32] K. M. Lyons, "Toward an understanding of the stabilization mechanisms of lifted turbulent jet flames: Experiments," *Progress in Energy and Combustion Science*, vol. 33, pp. 211–231, Apr. 2007.

[33] H. Yamashita, M. Shimada, and T. Takeno, "A numerical study on flame stability at the transition point of jet diffusion flames," *Symposium (International) on Combustion*, vol. 26, pp. 27–34, Jan. 1996.

[34] L. SU, O. SUN, and M. MUNGAL, "Experimental investigation of stabilization mechanisms in turbulent, lifted jet diffusion flames," *Combustion and Flame*, vol. 144, pp. 494–512, Feb. 2006.

[35] C. Lawn, "Lifted flames on fuel jets in co-flowing air," *Progress in Energy and Combustion Science*, vol. 35, pp. 1–30, Feb. 2009.

[36] E. Mastorakos, "Ignition of turbulent non-premixed flames," *Progress in Energy and Combustion Science*, vol. 35, pp. 57–97, Feb. 2009.

[37] A. L. Nán, M. Vera, and A. L. Sánchez, "Ignition, Liftoff, and Extinction of Gaseous Diffusion Flames," *Annu. Rev. Fluid Mech*, vol. 47, pp. 293–314, 2015.

[38] L. Vanquickenborne and A. van Tiggelen, "The stabilization mechanism of lifted diffusion flames," *Combustion and Flame*, vol. 10, pp. 59–69, Mar. 1966.

[39] R. C. Miake-Lye and J. A. Hammer, "Lifted turbulent jet flames: A stability criterion based on the jet large-scale structure," *Symposium (International) on Combustion*, vol. 22, pp. 817–824, Jan. 1989.

[40] A. Ramachandran, *Global Features of Flame Stabilization in Turbulent Non-premixed Jet Flames in Vitiated Coflow*. PhD thesis, 2015.

[41] R. Weber, J. P. Smart, and W. vd Kamp, "On the (MILD) combustion of gaseous, liquid, and solid fuels in high temperature preheated air," *Proceedings of the Combustion Institute*, vol. 30, pp. 2623–2629, Jan. 2005.

[42] A. Frassoldati, P. Sharma, A. Cuoci, T. Faravelli, and E. Ranzi, "Kinetic and fluid dynamics modeling of methane/hydrogen jet flames in diluted coflow," *Applied Thermal Engineering*, vol. 30, pp. 376–383, Mar. 2010.

[43] J. Aminian, C. Galletti, S. Shahhosseini, and L. Tognotti, "Numerical investigation of a MILD combustion burner: Analysis of mixing field, chemical kinetics and turbulence-chemistry interaction," *Flow, Turbulence and Combustion*, vol. 88, no. 4, pp. 597–623, 2012.

[44] S. R. Shabanian, P. R. Medwell, M. Rahimi, A. Frassoldati, and A. Cuoci, "Kinetic and fluid dynamic modeling of ethylene jet flames in diluted and heated oxidant stream combustion conditions," *Applied Thermal Engineering*, vol. 52, pp. 538–554, Apr. 2013.

[45] J. Zhang, C. R. Shaddix, and R. W. Schefer, "Design of model-friendly turbulent non-premixed jet burners for C 2+ hydrocarbon fuels," *Review of Scientific Instruments*, vol. 82, no. 7, 2011.

[46] E. D. Zeuthen, *Radiation Emissions from Turbulent Diffusion Flames Burning Large Hydrocarbon Fuels*. M.s., Oregon State University, 2015.

[47] J. a. Widegren Bruno, T.J., "Thermal decomposition kinetics of the aviation fuel Jet-A," *Ind. Eng. Chem. Res.*, vol. 47, no. 13, pp. 4342–4348, 2008.

[48] S. Okhovat, *Temperature Evolution of Spark Kernels in Quiescent and Crossflow Conditions*. PhD thesis, Oregon State University, 2015.

[49] D. R. Burgess, *Thermochemical Data*. Gaithersburg: National Institute of Standards and Technology, 2016.

[50] J. T. Nakos, "Uncertainty analysis of thermocouple measurements used in normal and abnormal thermal environment experiments at Sandia's Radiant Heat Facility and Lurance Canyon Burn Site," Tech. Rep. April, 2004.

[51] A. E. Lutz, "Chemkin II," 1994.

[52] A. E. Lutz, "SENKIN," 1994.

[53] R. J. Kee and A. E. Lutz, "OPPDIF," 1994.

[54] P. Middha and H. Wang, "Tranfit_new," 2002.

[55] H. Wang, R. Xu, D. F. Davidson, S. Banerjee, T. Bowman, and R. K. Hanson, "A experiment-based lumped model of jet fuel combustion at high temperatures," 2016.

[56] H. Wang, X. You, A. V. Joshi, S. G. Davis, A. Laskin, F. Egolfopoulos, and C. K. Law, "USC Mech Version II. High-Temperature Combustion Reaction Model of H2/CO/C1-C4 Compounds," 2007.

[57] T. Echekki and J. H. Chen, "High-temperature combustion in autoigniting non-homogeneous hydrogen/air mixtures," *Proceedings of the Combustion Institute*, vol. 29, pp. 2061–2068, Jan. 2002.

[58] T. Echekki and J. H. Chen, "Direct numerical simulation of autoignition in non-homogeneous hydrogen-air mixtures," *Combustion and Flame*, vol. 134, no. 3, pp. 169–191, 2003.

[59] A. Holley, Y. Dong, M. Andac, F. Egolfopoulos, and T. Edwards, "Ignition and extinction of non-premixed flames of single-component liquid hydrocarbons, jet fuels, and their surrogates," *Proceedings of the Combustion Institute*, vol. 31, no. 1, pp. 1205–1213, 2007.

[60] G. Carazzo, E. Kaminski, and S. Tait, "The route to self-similarity in turbulent jets and plumes," *Journal of Fluid Mechanics*, vol. 547, no. -1, p. 137, 2006.

[61] D. Han and M. Mungal, "Direct measurement of entrainment in reacting/non-reacting turbulent jets," *Combustion and Flame*, vol. 124, no. 3, pp. 370–386, 2001.

[62] B. B. Norheim, M. Bysveen, and M. Ditaranto, "Lift-off of methane jet flames in O2 / CO2 atmospheres," *Norwegian University of Science and Technology*, no. June, 2009.

[63] J. Boulanger, L. Vervisch, J. Reveillon, and S. Ghosal, "Effects of heat release in laminar diffusion flames lifted on round jets," *Combustion and Flame*, vol. 134, no. 4, pp. 355–368, 2003.

[64] R. L. Gordon, A. R. Masri, and E. Mastorakos, "Heat release rate as represented by [OH] x [CH2O] and its role in autoignition," *Combustion Theory and Modeling*, vol. 13, no. 4, pp. 645–670, 2009.

[65] R. L. Gordon, A. R. Masri, and E. Mastorakos, "Simultaneous Rayleigh temperature, OH- and CH2O-LIF imaging of methane jets in a vitiated coflow," *Combustion and Flame*, vol. 155, pp. 181–195, Oct. 2008.

[66] K.-O. Lee, C. M. Megaridis, S. Zelepouga, A. V. Saveliev, L. A. Kennedy, O. Charon, and F. Ammouri, "Soot formation effects of oxygen concentration in the oxidizer stream of laminar coannular nonpremixed methane/air flames," *Combustion and Flame*, vol. 121, no. 1, pp. 323–333, 2000.

[67] G. Freeman and A. Lefebvre, "Spontaneous ignition characteristics of gaseous hydrocarbon-air mixtures," *Combustion and Flame*, vol. 58, pp. 153–162, Nov. 1984.

[68] J. Kojima, Y. Ikeda, and T. Nakajima, "Spatially resolved measurement of OH*, CH*, and C2* chemiluminescence in the reaction zone of laminar methane/air premixed flames," *Proceedings of the Combustion Institute*, vol. 28, pp. 1757–1764, Jan. 2000.

[69] P. E. Dimotakis, "The mixing transition in turbulent flows," *Journal of Fluid Mechanics*, vol. 409, pp. 69–98, 2000.

[70] F. M. White, *Fluid Mechanics*. New York: McGraw-Hill, 7th ed., 2011.

[71] K. S. Pedersen, A. Fredenslund, P. L. Christensen, and P. Thomassen, "Viscosity of crude oils," *Chemical Engineering Science*, vol. 39, no. 6, pp. 1011–1016, 1984.

APPENDICES

Appendix A: Vaporized Fuel Viscosity Calculations

A.1 Calculation Procedure

Viscosity is a critical parameter for determining the Reynolds number. The kinematic and dynamic viscosities of large hydrocarbon fuels are generally well-characterized at or below room temperature, they have not been measured at higher temperatures around 300°C. In order to determine accurate Reynolds numbers for the central fuel jet in the JHC burner, a viscosity prediction method is required.

Pedersen et al. [71] used a corresponding states method involving the critical properties and molecular weights of pure hydrocarbons to determine a temperature and pressure dependent mixture kinematic viscosity. In this approach, methane is used as a reference fluid since its viscosity is well-characterized over a range of temperatures and pressures.

The final mixture viscosity is given by Equation A.1. Subscript 0 refers to the methane reference fluid, subscript c refers to the critical state, and subscripts i and j correspond to a given pair of hydrocarbon fluids of interest.

$$
\begin{aligned}
\mu_{mix}\left(P,T\right) = & \left(\frac{T_{c,mix}}{T_{c,0}}\right)^{-\frac{1}{6}} \left(\frac{P_{c,mix}}{P_{c,0}}\right)^{\frac{2}{3}} \left(\frac{MW_{mix}}{MW_0}\right)^{\frac{1}{2}} \frac{\alpha_{mix}}{\alpha_0} \times \\
& \mu_0\left(\frac{P \cdot P_{c,0}\alpha_0}{P_{c,mix}\alpha_{mix}}, \frac{T \cdot T_{c,0}\alpha_0}{T_{c,mix}\alpha_{mix}}\right)
\end{aligned}
\tag{A.1}
$$

The mixture critical temperature and pressure are given in Equations A.2 and A.3, where x represents the mol fraction of the i-th or j-th species, while T_c and P_c represent the i-th or j-th species critical temperature or pressure, respectively.

$$T_{c,mix} = \frac{\sum_i \sum_j x_i x_j \left[\left(\frac{T_{c,i}}{P_{c,i}}\right)^{\frac{1}{3}} + \left(\frac{T_{c,j}}{P_{c,j}}\right)^{\frac{1}{3}} \right]^3 [T_{c,i}T_{c,j}]^{\frac{1}{2}}}{\sum_i \sum_j x_i x_j \left[\left(\frac{T_{c,i}}{P_{c,i}}\right)^{\frac{1}{3}} + \left(\frac{T_{c,j}}{P_{c,j}}\right)^{\frac{1}{3}} \right]^3} \tag{A.2}$$

$$P_{c,mix} = \frac{8 \sum_i \sum_j x_i x_j \left[\left(\frac{T_{c,i}}{P_{c,i}}\right)^{\frac{1}{3}} + \left(\frac{T_{c,j}}{P_{c,j}}\right)^{\frac{1}{3}} \right]^3 [T_{c,i}T_{c,j}]^{\frac{1}{2}}}{\left(\sum_i \sum_j x_i x_j \left[\left(\frac{T_{c,i}}{P_{c,i}}\right)^{\frac{1}{3}} + \left(\frac{T_{c,j}}{P_{c,j}}\right)^{\frac{1}{3}} \right]^3 \right)^2} \tag{A.3}$$

A volumetric average and a weighted average of molecular weights are given in Equation A.4 since larger molecules have a larger affect on viscosity, they are given more weight in the mixture molecular weight given in Equation A.5.

$$\overline{MW_n} = \sum_i x_i MW_i \text{ and } \overline{MW_w} = \frac{\sum_i x_i MW_i^2}{\sum_i x_i MW_i} \tag{A.4}$$

Equations A.5 through A.8 are empirical relations for mixing rules determined from experimental curve fits of mixture viscosity data. They are used to determine the final mixture viscosity in Equation A.1.

$$MW_{mix} = \overline{MW_n} + 0.291 \left(\overline{MW_w} - \overline{MW_n} \right) \tag{A.5}$$

$$\alpha_{mix} = 1 + 7.747 \cdot 10^{-5} \rho_r^{4.265} MW_{mix}^{0.8579} \tag{A.6}$$

$$\alpha_0 = 1 + 8.374 \cdot 10^{-4} \rho_r^{4.265} \tag{A.7}$$

$$\rho_r = \frac{\rho_0 \left(\dfrac{T \cdot T_{c,0}}{T_{c,mix}}, \dfrac{P \cdot P_{c,0}}{P_{c,mix}} \right)}{\rho_{c,0}} \tag{A.8}$$

Detailed fuel composition data is available through a comprehensive two-dimensional gas chromatography analysis performed as part of the National Jet Fuels Combustion Program (NJFCP). 83 species are considered in the GCxGC results, but for the purpose of this work, these compounds are condensed down to 8 categories using weighted averages based on structural similarities shown in Table A.1.

Table A.1: Hydrocarbon structural categories used in fuel viscosity calculations

	A2	C4	C5
Alkylbenzenes	14.6%	0.3%	34.5%
Alkylnaphthalenes	2.4%	0%	0%
Cycloaromatics	3.3%	0.1%	0%
iso-Paraffins	27.0%	97.7%	48.2%
n-Paraffins	19.1%	0.2%	16.9%
Monocycloparaffins	24.4%	0.4%	0%
Dicycloparaffins	6.5%	0%	0%
Tricycloparaffins	0.2%	0%	0%

The weight percent reported for each compound is used to calculate weighted

averages of molecular weights and critical properties for each of the eight categories. These parameters are then processed using the method described above. The resultant fuel viscosities are reported in Table 3.1.

An excel document, a Matlab code, and an EES code are used to implement the viscosity calculations. The excel document contains all of the detailed fuel composition data and the calculations required to condense the information into 8 usable categories of compounds. The Matlab code reads in the distilled data from the excel sheet, then performs the calculations given in Equations A.1 through A.8. The EES code is used at the same time as the Matlab code for determining methane fluid properties at the conditions specified in Equations A.1 and A.8.

A.2 Relevant Code

```matlab
clear
clc

P = 101.3; %kPa
T = 573; %K

% Analysis based on VISCOSITY OF CRUDE OILS,
% Pedersen (Chemical Engineering Science
% Vol. 39, No. 6, pp. 1011—1016
% Use with Fuel Composition and Critical Properties.xlsx
% AND Methane Corrected Viscosity.EES

data = xlsread('Fuel Composition and Critical Properties'...
    ,'Distilled Properties','J16:M23');
x = data([1 3 4 5 6],1)/100; %Mol Fraction
MW = data([1 3 4 5 6],2); %Average Molecular Weight
Tc = data([1 3 4 5 6],3); %Critical temperature
Pc = data([1 3 4 5 6],4)*1000; %Critical Pressure (Convert to kPa)


for i = 1:length(x)
    for j = 1:length(x)
        num(i,j) = x(i)*x(j)*((Tc(i)/Pc(i))^(1/3)...
            + (Tc(j)/Pc(j))^(1/3))^3*(Tc(i)*Tc(j))^(1/2);
        den(i,j) = x(i)*x(j)*((Tc(i)/Pc(i))^(1/3)...
            + (Tc(j)/Pc(j))^(1/3))^3;
    end
end

TcMix = sum(sum(num))/sum(sum(den));
PcMix = 8*sum(sum(num))/(sum(sum(den)))^2;

MWn = sum(x.*MW);
MWw = sum(x.*MW.^2)/MWn;
MWmix = MWn + 0.291*(MWw — MWn);


Tc0 = 190.6; %K (Methane Critical Temperature, from EES)
```

```matlab
Pc0 = 4599; %MPa (Methane Critical Pressure, from EES)
Trho0 = T*Tc0/TcMix; %Corrected T for Methane Density
Prho0 = P*Pc0/PcMix; %Corrected P for Methane Density

rho0 = 3.028; %Density of Methane from EES
rhoc0 = 136.1; %Critical density of Methane from EES
rhoR = rho0/rhoc0;

alphaMix = 1 + 7.747e-5*rhoR^4.265*MWmix^0.8579;
alpha0 = 1 + 8.374e-4*rhoR^4.265;

Pmu0 = P*Pc0*alpha0/(PcMix*alphaMix); %Corrected T
Tmu0 = T*Tc0*alpha0/(TcMix*alphaMix); %Corrected P

MW0 = 16.044; %Molecular weight of methane
mu0 = 0.000006283; %Corrected viscosity of Methane from EES
mu_mix = (TcMix/Tc0)^(-1/6)*(PcMix/Pc0)^(2/3)...
    *(MWmix/MW0)^(1/2)*(alphaMix/alpha0)*mu0; %kg/m-s
```

Appendix B: Coflow Flow Rate Calibration and Uncertainty Analysis

B.1 Pressure Transducer Calibration

To accurately meter each of the four coflow gasses (air, nitrogen, methane, and hydrogen), orifice flow meters are used as described in Section 3.2. All eight pressure transducers were calibrated with an Omega PCL-1B in a seven-point calibration. A slope and offset were determined from a linear fit of the transducer voltage to sensed pressure data, which for all transducers had an R^2 value of 1. A sample calibration curve is provided in Figure B.1 for a 60 psig transducer.

The slopes and offsets of all eight transducers are tabulated in Table B.1 for each serial number.

B.2 Orifice Flow Meter Calibration

Once the pressure transducers were calibrated, they were installed into the orifice flow meters. Each orifice was then calibrated using air as a working fluid. It was found through a secondary experiment using methane as the working fluid that calibration with air provides good agreement with measured flow rates of the actual gasses when the differences in fluid properties are taken into account. Compressed
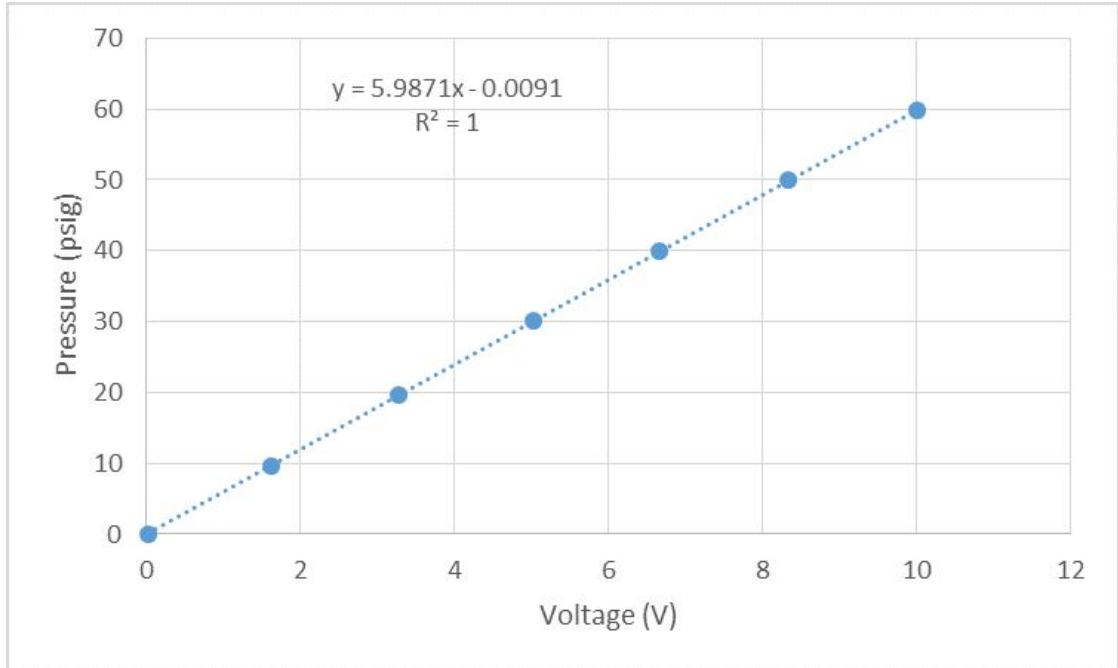
Figure B.1: Calibration curve for pressure transducer serial number 5082801055

Table B.1: Pressure Transducer Calibration Constants

Label	Serial Number	Pressure Range (psig)	Slope	Offset
1	5091818320	30	2.9964	-0.0156
2	5091907047	30	3.0001	-0.0207
3	5082801048	60	6.0211	-0.0445
4	5082801059	60	6.0096	0.0676
5	5082801055	60	5.9871	-0.0091
6	5082801044	60	5.9965	0.0776
7	5111705110	100	9.9789	0.0982
8	5111705115	100	9.9892	-0.1421

air from the building supply was fed through each orifice at a constant pressure. The volumetric flow rate of air was measured either with a dry test meter (Singer DTM-200) or bubble gilibrator (Bilian D800286). The methane and hydrogen orifices run in a choked configuration and were calibrated with the gilibrator. The air and nitrogen orifices run unchoked and were calibrated with the dry test meter.

The pressure readout of both the upstream and downstream transducer were recorded while the flowrate was measured, typically for about 3-5 minutes. The average pressure was calculated from the recording, with a typical standard deviation of 0.2 psig, which occurs due to slight pressure fluctuations. This is useful in determining how variable the flow rates will be during operation. The measured absolute upstream pressure and pressure ratio are then used in combination with the measured flow rate to calculate the C_dA, or orifice cross-sectional area multiplied by the discharge coefficient. The C_dA is calculated by rearranging the equations for choked and unchoked flow of a perfect gas through an orifice, which are given in Equations B.1 and B.2 respectively. Subscript 1 corresponds to a condition upstream of the orifice, while subscript 2 corresponds to a condition downstream of the orifice.

$$\dot{m} = C_dA \cdot P_1 \sqrt{\frac{\gamma}{\bar{R}T_1}\left(\frac{2}{\gamma+1}\right)^{\frac{\gamma+1}{\gamma-1}}} \tag{B.1}$$

$$\dot{m} = C_dA \cdot \rho_1 \sqrt{2\bar{R}T_1 \frac{\gamma}{\gamma-1}\left(\left(\frac{P_2}{P_1}\right)^{\frac{2}{\gamma}} - \left(\frac{P_2}{P_1}\right)^{\frac{\gamma+1}{\gamma}}\right)} \tag{B.2}$$

A curve fit is obtained for upstream pressure vs C_dA using data points from a

range of flow rates for each orifice. Upstream pressure was chosen as the independent variable in these curve fits because it produced the most well-behaved trend compared to other options. The curve fit was performed using the Matlab curve fit toolbox in order to specify the form of the desired equation. The general form is provided in Equation B.3, and matched the trend very well, with R^2 values greater than 0.93 in all cases.

$$C_d A = a \left[1 - exp \left[-b \cdot P_1 \left(psia \right) + c \right] \right] \tag{B.3}$$

Once the $C_d A$ curve fits were obtained, the mass flow rate of each gas could be metered using pressure and temperature measurements along with the appropriate fluid properties (γ and MW).

## B.3   Orifice Flow Meter Uncertainty

A Kline-McClintock uncertainty analysis was performed on each orifice to ensure that the flow of each gas was metered to a reasonable accuracy, ideally to within 5% or better of the reported value. Bias and repeatability error from measured pressures, temperatures, and flow rates were considered. The error introduced by the $C_d A$ curve fit was also taken into account.

A plot was generated to visualize the $C_d A$ calibration and corresponding errors associated with both the data and the curve fit itself. If the curve fit confidence bounds lie within the error bars of the calibration data, the error introduced via the curve fit is bounded by the error of the measurements. This is the desired

outcome of the calibration. The plots are shown in Figure B.2.
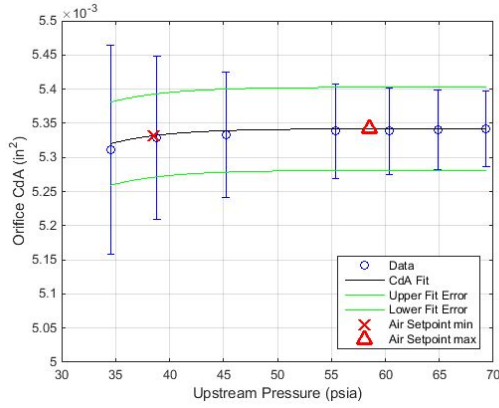
(a) Air
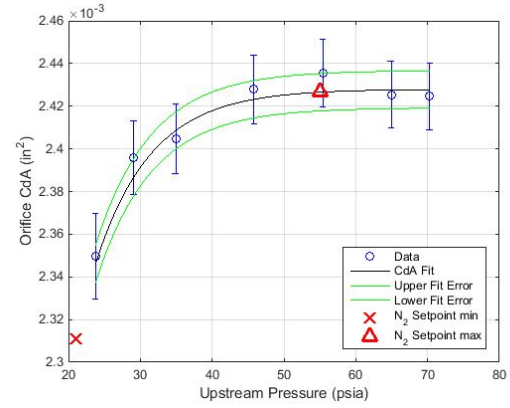
(b) Nitrogen
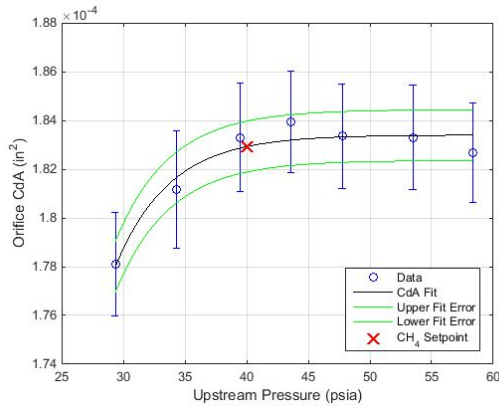
(c) Methane

(d) Hydrogen

Figure B.2: C_dA curve fits for each orifice

The methane and hydrogen plots in Subfigures B.2c and B.2d show good agreement with the curve fit and uncertainty of measurement, indicating that the curve fitting procedure has little effect on the error of metering the fuel gas. Air and nitrogen still provide good agreement, but the curve fits are not as accurate in

these cases. The difference can be attributed to the unchoked operation of the air and nitrogen orifices, as two pressure measurements are required. The assumption that the C_dA depend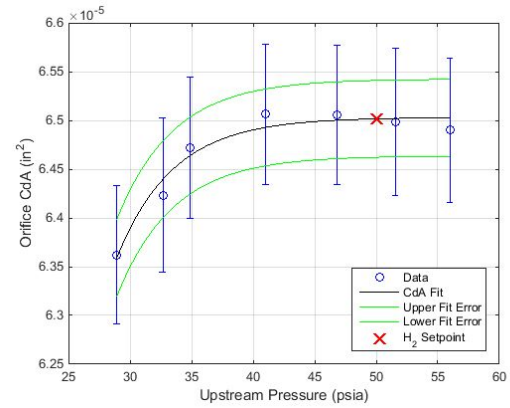s only on the upstream pressure is not as good in for these orifices, contributing to the larger error. In addition, the dry test meter is not as accurate as the gilibrator, further increasing the calibration error. The lowest nitrogen setpoint lies just outside of available data, but within 3% of the mean C_dA assuming the curve fit still applies at this location. Therefore, the accuracy lost by a small amount of extrapolation is negligible.

The final uncertainties in the mass flow rates are presented as percentages of the nominal values in Table B.2. The maximum uncertainty typically occurs at the lower end of the flow rate calibration range. For most of the setpoints actually used during testing, the average uncertainty value reported in Table B.2 is more applicable.

Table B.2: Final Mass Flow Uncertainties

	Max	Average
Air	3.8%	2.5%
Nitrogen	1.6%	1.4%
Methane	1.4%	1.4%
Hydrogen	1.5%	1.5%

The effect of calibrating with air instead of the final working gas was found to be negligible through a secondary experiment performed with methane. The mass flow results from the gilibrator were within the uncertainty of those calculated using the air calibration.

Appendix C: Liquid Fuel Orifice Calibration

The liquid fuel orifice is calibrated by performing a catch and weigh experiment using actual jet fuels, unlike the gas flow orifices which were calibrated using air as a surrogate fluid. The liquid fuel pressure regulator is adjusted to a set value and the fuel discharge is collected for a known length of time. The cumulative discharge is weighed and the average mass flow rate determined by dividing the result by the collection time. The differential pressure from the Validyne readout is recorded. The reading remained constant over several minutes for a given regulator set point. This is done for several flow rates and the results plotted in Figure C.1.
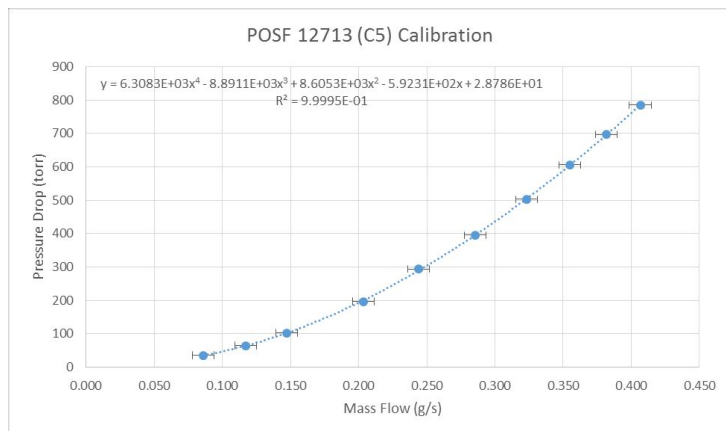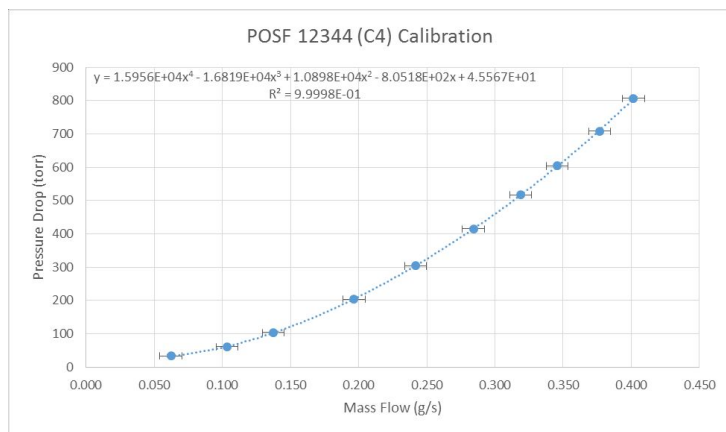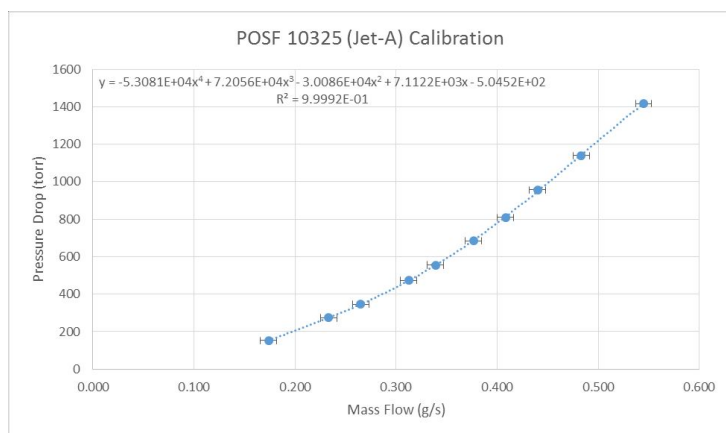
Figure C.1: Fuel orifice calibrations using O'Keefe Controls IC-4006-09-SS performed using a catch and weigh technique.

Appendix D: Laser Background and Miscellaneous Information

D.1   Laser System

A tunable dye laser (Lambda Physik FL 3002) pumped with a W-switched Nd:YAG laser (Continuum Custom) was used to perform OH PLIF on the MILD reaction zone. A wavelength of 283.222 nm was selected to excite the $A - X(1,0)Q_1(7)$ transition of OH based on work done previously by [5]. This excitation scheme is widely used in OH PLIF. The Nd:YAG laser operates in frequency doubled mode at a 532 nm wavelength with an average pulse energy of 200 mJ as measured by a thermopile power meter (Mentor MA-10). The Nd:YAG laser is fired at 20 Hz to achieve thermal equilibrium conditions in the laser heads, providing a more stable output.

The 532 nm beam is fed into the dye laser, where the high power beam is used to excite laser emission in Rhodamine 590 Chloride dye. The 566 nm output of the dye is frequency doubled, producing the required 283.222 nm light. The laser wavelength is verified by scanning the diffraction grating until the strongest PLIF signal is obtained near the desired wavelength. It would be desirable to aquire a wavemeter to not only verify that the wavelength is correct but also to measure the bandwidth of the laser light. Residual fundamental light is rejected using the four-prism pellin-broca array to separate the unwanted 566 nm wavelength. The

UV beam exits the dye laser and passes through a three-lens telescope that creates a laser sheet for PLIF diagnostics. The average pulse energy at 283.222 nm is around 2.5 mJ when the lasers are well-aligned and optimized for beam power. Alignment must be checked and adjusted periodically to ensure adequate beam energy is being delivered. About one percent of the beam is split off to be read by a photodiode, which measures the relative shot energy of each laser pulse. More detail is provided on the photodiode in Section E. An overview of the laser system is given in Figure D.1.

A pulse/delay generator (Stanford Research DG535) acts as a master clock for the entire laser/camera system. It directly drives the Nd:YAG laser flashlamp fire command, Q-switch power command, and camera gate command, while triggering the secondary timing system contained in the power measurement box discussed in Section E. A centralized timing scheme ensures that each laser pulse is timed exactly with the camera gate pulse so that the PLIF signal (which only lasts for a few nanoseconds) is captured by the camera.

D.2   PLIF Data Processing

PLIF measurements are made using the same Andor iStar 334t ICCD camera used for chemiluminescence measurements. The same 310 nm bandpass filter is used to reject the 283.222 nm laser light while allowing the laser excited OH flourescence near 310 nm to pass through to the camera sensor. The camera field of view is set based on the desired area to be imaged, with smaller window sizes allowing for
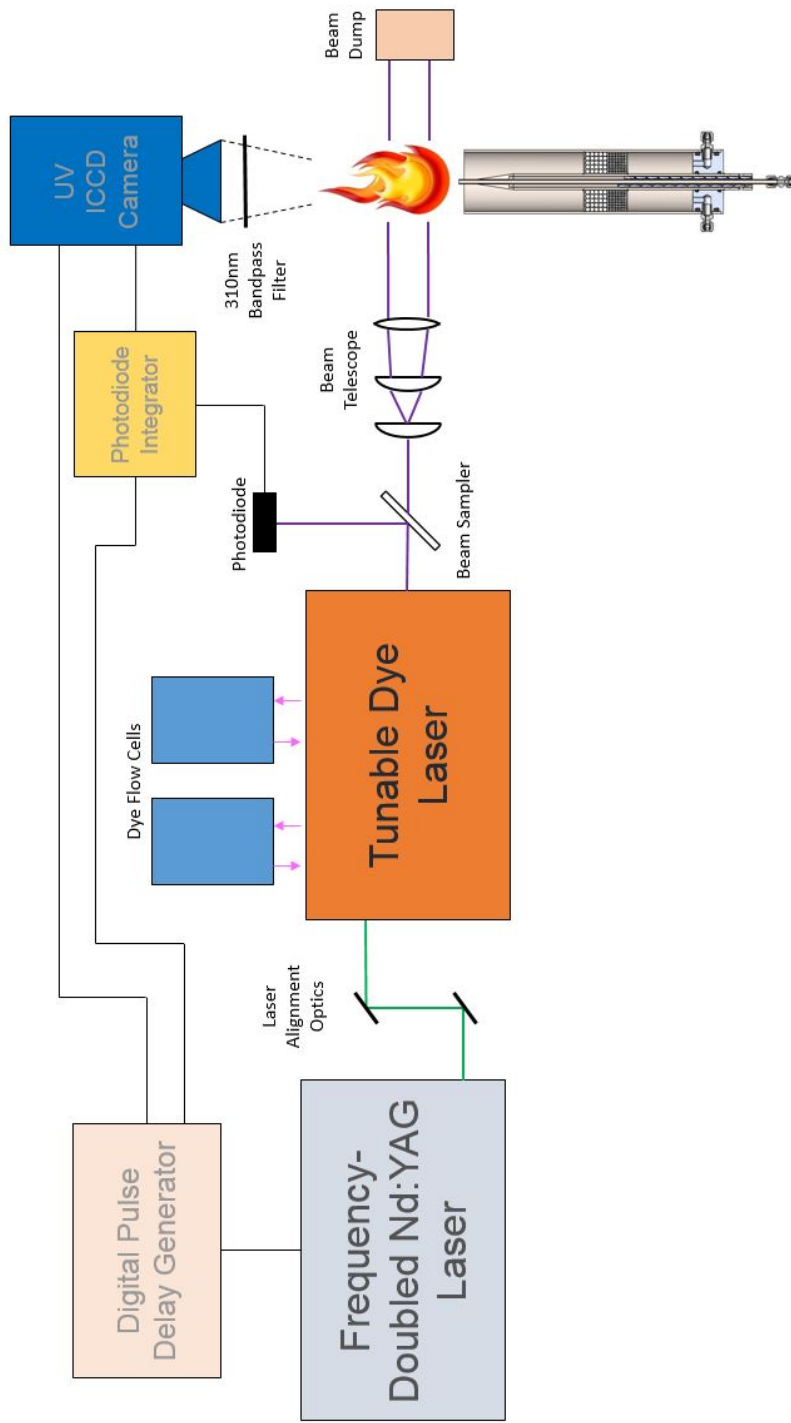
Figure D.1: Schematic of Laser System

faster image collection. The field of view required for PLIF is generally smaller than the field of view used for chemiluminescence measurements due to the relatively small size of the laser sheet. The camera is run in externally triggered mode to allow synchronization with the laser output via the DG 535 as described in Section D.1. The gate width is set to 6 ns and the gate delay is set to 338.088 μs. Output A must be enabled in order for the camera to send a signal to the photodiode integration box that it has captured an image. The delay is set to 0 s and the width is set to 10 ms.

The DG 535 has a number of settings that must be input correctly for the external triggering scheme to work. The trigger type must be set to Line, which triggers a new delay cascade cycle using the AC power line as a trigger source. The output impedance must be set to HighZ. Output A drives the camera triggering, output A⎍B triggers the Nd:YAG laser flashlamps, output A⎍B triggers the photodiode integration box, and output C⎍D triggers the Nd:YAG laser Q-switch. The output delays use the following settings: A=B- 10 μs, B=C- 328 μs, C=D- 10 μs, and D=T+ 45 ms. The DG 535 will not accept new trigger events until all current delays have been completed. By setting the D channel to a 45 ms delay time, a 20 Hz trigger duty cycle is derived from the 60 Hz AC power frequency. For Nd:YAG external triggering to work, the small blue box on the rear of the laser electronics rack must be turned on and the Q-switch BNC cable connected to the Ext Q SW IN port on the rear of the main laser controller. To run in manual mode using the corded laser remote, the blue box must be turned off and the external Q-switch BNC cable must be disconnected.

The burner control Labview GUI also handles PLIF shot power data collection using the photodiode integration box DAQ. The DAQ reads the voltage on the integration circuit at 1000 Hz, which allows it to resolve the integrated laser shot power. The resulting signal is saved to a .lvm file for processing. At the same time, the DAQ records the camera output signal so that each PLIF image can be matched to the shot power in post processing. A Matlab script is used to read in the combined camera and photodiode output. The code then determines the shot power of each laser pulse in the dataset, keeping only the data for pulses where an image was acquired. The code reads in the PLIF image data and normalizes each image with the laser power reading. The normalized images may now be directly compared on an intensity basis.

D.3   Nd:YAG Laser

The Nd:YAG laser is a powerful, yet fragile piece of equipment and should be treated with respect. Regular maintenance and careful adherence to the operating procedures covered in Section ?? will ensure user safety and a long life for the laser. It is a custom unit designed and built by Continuum, made in 1991. Continuum has long since discontinued servicing this model, however a third party company called Directed Light provides repair services when we cannot fix issues ourselves. They also stock many replacement parts.

D.3.1   Principles of Operation

The Nd:YAG laser generates a pulsed output beam in either 532nm green (frequency doubled mode) or 355nm ultraviolet (frequency tripled mode). The laser is typically pulsed at 20Hz, although it can operate at lower frequencies or in single shot mode. To generate the laser beam, a Neodymium-doped Yttrium Aluminum Garnet (Nd:YAG) rod is optically pumped using a high-intensity arc lamp. The arc lamps run at very high voltages and must be actively cooled with deionized water. The rod lases at a low power level along its longitudinal axis when excited by the arc lamp flash. To increase the power, feedback mirrors are used to pass the beam back and forth through the rod many times, with a portion of the beam escaping through a partially transmitting mirror on one end of the optical resonator cavity. A notional oscillator cavity is depicted in Figure D.2.

To achieve extremely short and repeatable pulse lengths, a device called a Q-switch is used inside the cavity in combination with a polarizer and quarter wave plate. The Q-swtch is a special crystal that produces a quarter wave rotation (45) in any photons passing through it while in the on position and does not alter the light when off. In conjunction with the quarter wave plate, the Q-switch produces 180 of rotation when in the on position since the light passes through both elements twice as it is reflected through the cavity. The light emitted from the Nd:YAG rod is horizontally polarized and is rejected by the polarizer inside the cavity unless the Q-switch is activated by a tightly controlled high voltage pulse. See page 3-12 in the Continuum manual for more information.

Nd:YAG solid-state laser

Highly reflective mirror

Flashlamp (pump source)

Partially reflective mirror

Laser output

ND: YAG crystal (laser medium)
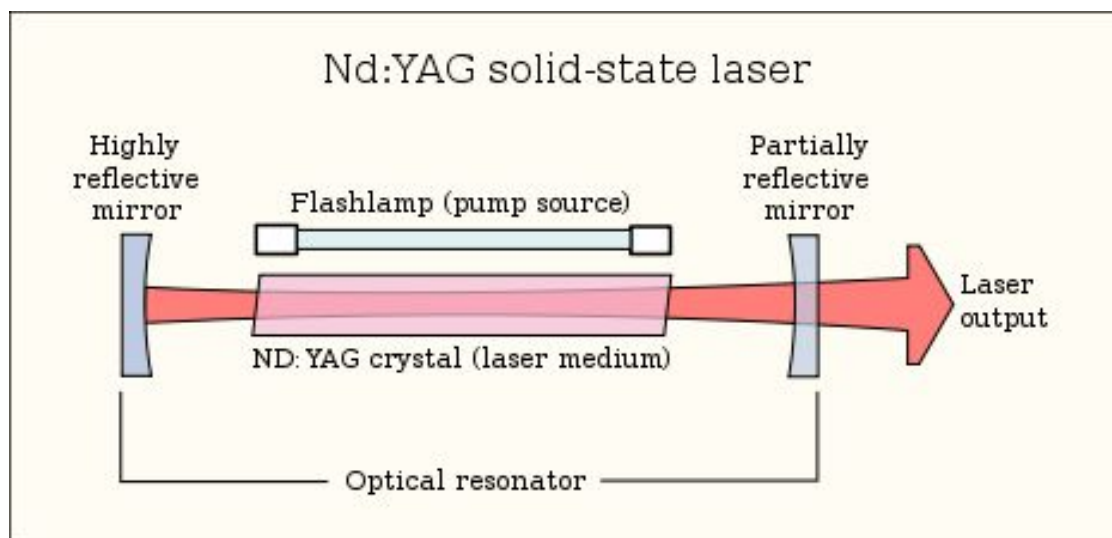
Optical resonator

Figure D.2: Depiction of Nd:YAG Laser Oscillator Cavity

Once the laser light exits the optical cavity through the partially reflective mirror, it passes through a series of beam shaping and turning optics, most notably a Faraday Isolator. It acts as an optical check valve, preventing upstream reflections from propagating backwards to the oscillation cavity and interfering with the feedback process. The beam passes through two additional laser heads, each with two flash lamps and a corresponding Nd:YAG rod. These heads serve as the pre amplifier and power amplifier, substantially increasing the beam energy. After each of these laser heads, a two lens beam telescope is used to shape the substantially larger beam into a tight and coherent focus. Up to this point in the laser, the beam has been entirely in the infrared at 1064 nm. It now enters a frequency doubling crystal, where it is converted into 532 nm light. Much of the power loss occurs during this step. If desired, a second crystal can be used to run in 355

nm mode with additional power losses. The beam is directed onto two sequential dichroic mirrors. These mirrors are highly reflective to 532 nm light but partially transmit most other wavelengths. The frequency doubling crystals do not convert 100% of the infrared laser into visible light, so the dichroic mirrors filter out the remaining infrared portion of the beam while directing the green light to the laser cabinet outlet. To run in frequency tripled mode, the 532 nm dichroics must be swapped out with the 355 nm dichroics that reside inside the laser cabinet on separate mounts.

D.3.2   Maintenance Schedule

Preventative maintenance of the laser is required on a regular basis to prevent more costly repairs in the event of an actual failure. The schedule in Figure D.3 should be followed whenever the laser is in regular use. If the laser is inactive for a long period of time, a check should be performed before resuming regular operation. Instructions for performing the actions laid out in the schedule can be found in Section 4 of the Continuum manual. It is a good idea to keep spare flash lamps, DI filter cartridges, and laser head O-rings on hand to avoid having to wait for parts that have long lead times.

	Each Month	Every 6 Months	Every 12 Months
Check System Alignment	X		
Clean/Inspect Optics	X		
Change DI Filter in Cooling Unit		X	
Replace Flash Lamps		X	
Replace Laser Head O-Rings			X

Figure D.3: Nd:YAG Maintainance Schedule

D.3.3   Operating Procedures

The operating procedures are laid out in detail in Section 2 of the Continuum manual. A brief overview of startup, shutdown, emergency shutdown, and normal operation procedures are given here.

D.3.3.1   Startup

1. Open building water ball valve under West sink and globe valve on North side of the island. Ensure that outlet hose will drain into the West sink and that a trickle of water is flowing.

2. Switch on main electronics rack circuit breaker.

3. Make sure that the internal cooling loop is working and that there are no

leaks. Allow DI water to flow for at least 10 minutes before operating the laser, as the filter must remove the ions the water has picked up from the system in order to avoid a dangerous electrical short scenario.

4. Turn on desired power supplies (upper for running with the oscillator only, both for full power operation with the pre-amplifier and power amplifier).

5. Turn key into off position, this is actually on, it is mislabeled.

6. Laser is ready to operate when main menu appears.

D.3.3.2   Normal Operation (via remote)

The Nd:YAG rods must be allowed to thermally stabilize before lasing can occur without damaging the rods.

1. Run program 1 by pressing the Auto/Manual key, then activate PGM1 by pressing the activate key, then press the start key. The lamps will begin flashing but lasing will not occur.

2. Allow the laser to run PGM1 for 5 minutes to thermally stabilize the rods and lamps.

3. When ready to fire the laser, two modes are available: single shot mode and continuous firing mode. PGM2 is for single shot mode and PGM3 is for continuous shooting.

4. In either mode, operation is mostly the same. When ready to fire, press the shutter key to remove the shutter safety interlock. Verify that the shutter light is on and that the shutter has moved out of the optical cavity.

5. Press the Q-switch key to turn on the Q-switch. In continuous firing mode (PGM3) lasing will occur at the specified rep rate. In single shot mode, nothing will occur.

6. To fire in single shot mode (PGM2), press the fire key when both the shutter and Q-switch are open.

D.3.3.3   External Triggering Mode

When performing PLIF measurements in conjunction with the UV camera, external triggering must be implemented to synchronize the laser pulses with the camera shutter in order to capture the laser sheet at maximum power in the region of interest. Using an external timing source (SRS DG535) overrides the normal laser triggering logic so care must be taken to not operate the laser at exceedingly high rep rates (nothing above 20Hz). The laser requires two external inputs in order to operate: a flashlamp fire command and a Q-switch open command. The timing of these commands is very important and is detailed in Figure D.4.

It is recommended to verify the timing of the SRS DG535 output using an oscilloscope before applying the logic to the laser, as the logic is not always intuitive. The unit uses the 60Hz line input as a trigger source, so it will trigger every 1/60
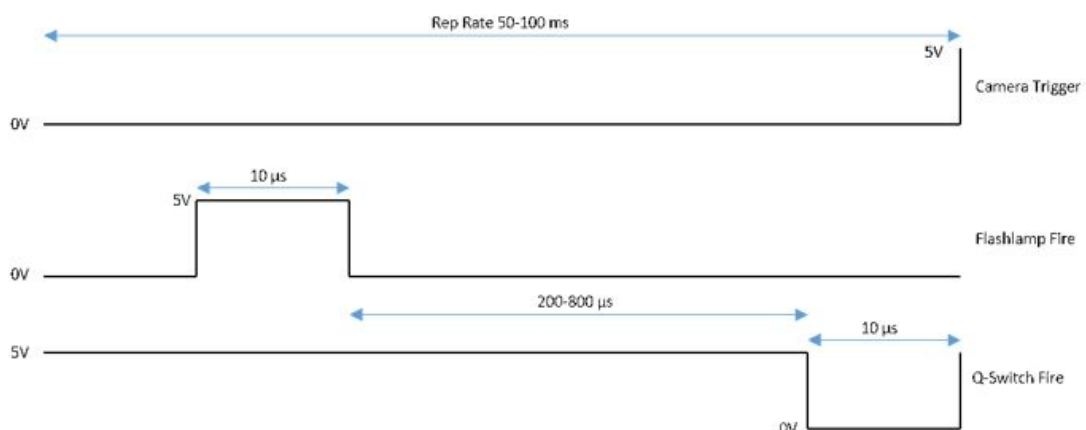
Figure D.4: Nd:YAG External Triggering Timing Diagram

of a second. However, it will ignore all triggers that occur while any of the delay outputs are active. By setting the D output to a desired length, a rep rate below 60Hz can be set up with very little jitter. For example, to get a 20Hz rep rate, set the output D delay to T0+ 45 ms. This generates a trigger rate of 20Hz. It is wise to verify the output with an oscilloscope before using on the laser.

The flashlamps are triggered by a 10 microsecond long, 5V TTL pulse typically delivered from DG535 output AB+ to the small blue box velcroed to the back of the laser electronics cabinet. This box also contains a 5V power line that is tapped off of a 5V power supply inside the control unit rack. The AB output produces a pulse that begins at the A delay time and ends at the B delay time. The Q-switch is triggered by a 10 microsecond long, 0V TTL pulse (down from a nominal 5V) delivered from DG535 output CD- to the external Q-switch port.

The Andor camera triggers on the downslope of a 5V TTL signal, which occurs

at the end of the Q-switch pulse from the DG535 output D. Output D also signals the end of the trigger cycle. The internal gate delay feature in the camera software is then used to adjust the time between the laser firing and the camera shutter to get the best possible image.

1. Set up all of the appropriate delay times on the SRS DG535 before powering up the laser to ensure the lamps wont be fired at an excessively high rep rate.

2. Power on the laser according to the startup procedure.

3. Activate PGM1 but DO NOT press the start button.

4. Turn on the SRS DG535 and flip the on switch on the blue box attached to the back of the electronics rack. This enables the TTL circuit. The lamps will begin flashing at the rep rate specified by the DG535.

5. Allow the lamps to thermally stabilize for 5 minutes while the shutter remains closed.

6. When ready to fire the laser, switch to PGM2 or PGM3 and open the shutter. The shutter will not open in PGM1. Since the Q-switch is being told to fire by the DG535, lasing will start immediately.

7. If it hasnt already been done, adjust the camera gate delay settings until the desired image is obtained. See Andor iStar manual for info on camera operation and settings.

D.3.3.4   Shutdown

1. To stop the laser in both normal shutdown and in emergency shutdown mode, press the stop key when the laser is in operation to halt the flashlamp and Q-switch pulses. If in externally triggered operation, power down the SRS DG535. Do not turn off the laser circuit breakers until the lamps have been given sufficient time to cool down.

2. When the lamps are cool, turn the keyswitch into the on position to disable the firing logic (actually off, it is mislabeled)

3. Turn off the power supply circuit breakers.

4. Turn off the main circuit breaker.

5. Turn off the cooling water ball valve and globe valve located on the central island.

D.4   Dye Laser

The Lambda Physik FL3002 Dye Laser is a device that uses the Nd:YAG laser as a pump source in order to drive an organic dye solution to lasing operation. The dye laser allows for very fine adjustments to the output wavelength of light, up to a picometer of wavelength resolution. The dye laser can only output up to 50% of the input Nd:YAG laser power. The output beam is nicely conditioned and well-collimated.

D.4.1   Principles of Operation

Compared to the Nd:YAG laser, the Dye laser is very compact and automated. Once alignment of the Nd:YAG laser has been completed, all control is performed using the front panel. If the dye laser or Nd:YAG laser is ever moved, alignment will need to be performed again. The Nd:YAG laser enters the dye laser cabinet from the left side. There is a normally-closed shutter that will not allow the pump beam to enter the cabinet when either the dye laser power is off or the cover is off. The cover interlock can be defeated by pressing and holding the button on the rear left corner of the laser case. The pump beam passes through the oscillator beam splitter that sends a portion of the pump beam to the oscillator flow cuvette while the majority of the pump beam passes through. It then is reflected by two folding mirrors to a pre-amplifier beam splitter than sends another portion of the pump beam to the oscillator flow cuvette at a different angle than the initial beam splitter. The remaining pump beam progresses through additional shaping and turning optics and into the main amplifier flow cuvette.

Dye in the oscillator cuvette acts as both the gain medium in the laser oscillator cavity and as a pre-amplifier once the laser light has been tuned to the appropriate frequency. Tuning is accomplished via an adjustable diffraction grating, which selects one frequency of light to reflect back into the oscillator cavity, where that frequency is amplified. The laser is relatively weak at this point (about 5 mW) and required amplification. This is accomplished by passing the tuned beam through the region where the second portion of the pump laser intersects the oscillator

cuvette. This increases the available laser power to an intermediate level, about 40 mW. Final amplification is performed when the tuned light intersects the majority of the pump beam power in the main amplifier cuvette. The average power should now be approximately 325 mW if the laser is well-aligned. Frequency doubling must now occur to obtain UV laser light. A movable crystal performs the frequency conversion, which is very sensitive to the crystal angle. It must be adjusted to achieve maximum power using the dye laser control panel. The conversion is not 100% efficient, so a pellin-broca prism array is used to separate the fundamental wavelength from the doubled wavelength. To visualize the UV beam, place a piece of plain white paper into the beam path. It should flouresce bright blue when the crystal is tuned properly. UV laser power (for a wavelength of 283 nm) should be at least 30 mW.

Appendix E: Single-Shot Power Measurement Device

The total energy delivered by each laser pulse must be taken into account due to the proportionality of the PLIF signal to the laser power. The Nd:YAG laser used in this work exhibits significant power variation between shots, sometimes on the order of 50% variation in shot power. A photodiode integration device was designed and built to measure the total shot power of each laser pulse while the laser operates in continuous firing mode. The circuit diagram is shown in Figure E.1. Each laser pulse lasts approximately 10 nanoseconds and the pulses occur at 20Hz, making measuring the single-shot pulse energy quite difficult due to the data acquisition speeds (around 1 GHz) required to fully resolve a pulse with a FHWM of 10 ns. A reversed biased, fast response time photodiode (Thorlabs DET10A) and a precision current integration chip (Texas Instruments IVC102) were combined to resolve the total shot energy while only requiring a DAQ sampling rate of 1000 Hz. The resulting pulse energy measurement was used to normalize the PLIF signal, so an accurate measurement of absolute power was not required.

The custom photodiode integrator requires several support systems to function properly. A linear power supply provides clean, regulated power at +/- 15 VDC to the integration chip. It also has an auxiliary 5 VDC rail to power two timers (Texas Instruments NE556) running in monostable mode. The DG535 master timer triggers the 556 timers, which control the reset and hold functionality of the
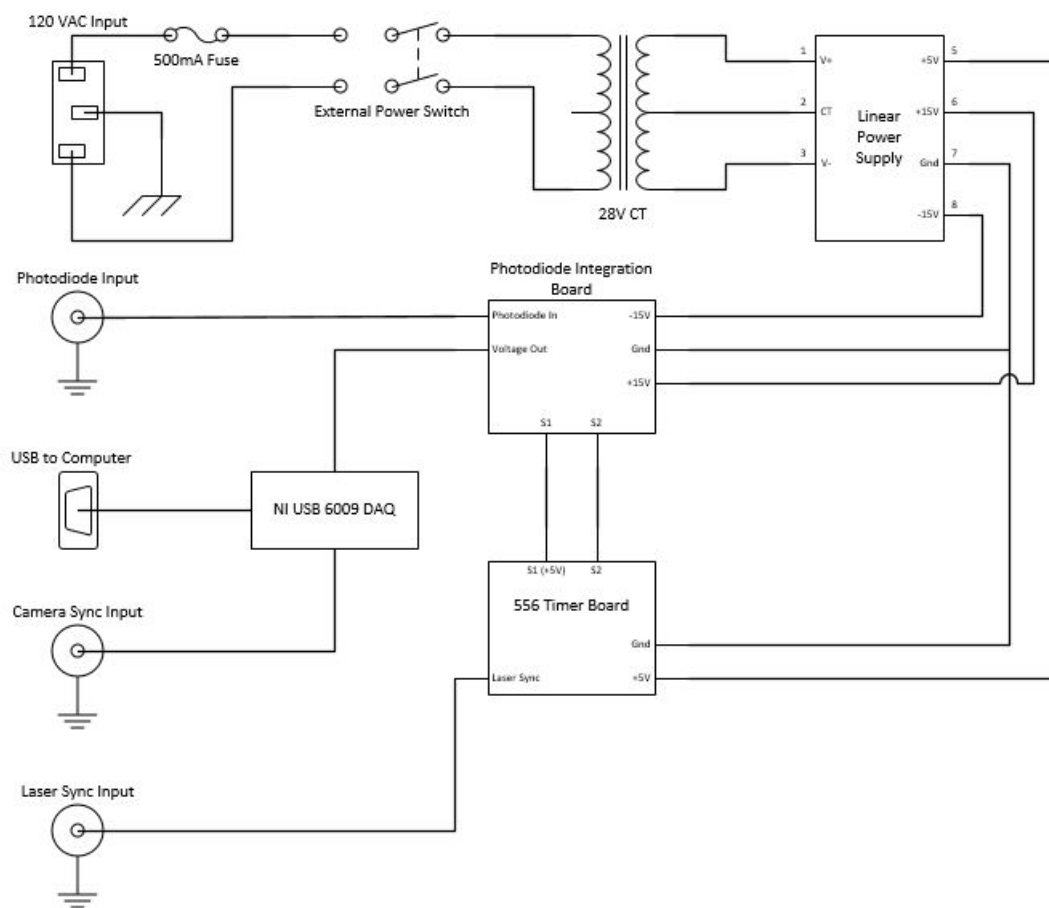
Figure E.1: Schematic of Laser Power Measurement Device

integration chip. The first stage of each 556 timer acts as a delay for the second stage, which energizes one of two solid state switches (S1 and S2) contained in the integration chip.

In the current configuration, the second timer is not used and S1 is held open with a constant +5 VDC. In this mode, the chip constantly integrates the ambient

light detected by the photodiode. When light from the dye laser is detected, a sharp increase in the integrator voltage is seen on the DAQ voltage readout. The difference in voltage between these two points represents the total shot power detected by the photodiode. Every 0.05 seconds, the integrator is reset by the 10us pulse from the 556 timer and the readout voltage drops to near zero. The camera is only able to capture images at around 1.5Hz (depending on the aquisition settings), so a synchronization pulse is output from the camera to the photodiode DAQ every time an image is acquired. The camera images can then be matched to the corresponding laser shot power measurement in post processing, where the power measurement is used to normalize the PLIF signal.

Appendix F: Running Senkin and OPPDIF Codes

The chemical kinetic mechanism files provided by Hai Wang can not be run correctly on the commercial version of Chemkin, as they use a non-standard transport property fit method. A modified version of the opposed flow flame simulation code (OPPDIF) is required to use the transport property fits correctly. A modified version of Senkin is not required, as transport properties are not used in a zero dimensional homogeneous reactor model. Unfortunately Senkin and OPPDIF are Fortran packages that are not at all intuitive to run. A brief overview of the required software, files, and syntax is presented here.

Microsoft Visual Studio Community 2015 (or better) and the Intel x64 Fortran/C++ compilers are required to install and run the chemical kinetics processing (CHEM), transport property fitting program (TRAN), Senkin, and OPPDIF routines. The 2016 Intel Fortran/C++ compilers are used. A free installation of Visual Studio Community can be found on the Microsoft website while the Intel compilers can be found on the Intel website and are free to students.

A .make file must be executed via the command line in order to install Senkin along with the modified CHEM, TRAN, and OPPDIF executables (received from Hai Wang). To execute the make file, complete the following steps.

1. Install Microsoft Visual Studio and the Intel Fortran/C++ compiler. Visual studio may direct you to specify a target machine type via command prompt

to initialize the compiler. Be sure to target "intel64" as the machine type, as the modified chemkin programs are written for 64 bit machines.

2. Open a command prompt window running the Intel Fortran/C++ environment. This is found in the appropriate Intel folder in the start menu.

3. Navigate to the directory containing the make file using the "cd" command.

4. Type "nmake -f make.WIN" to run the make file. It should not display any errors if execution is successful. There will now be several .exe, .obj, and .lib files in the working directory. The files of interest are chem.exe, tran.exe, senkin.exe, and oppdif.exe.

Both Senkin and OPPDIF require the CHEM program to run preprocessing steps on the chemical kinetics files. Two files are needed: chem.inp and therm.dat. These files contain chemical reaction mechanisms and NASA thermodynamic polynomial coefficients, respectively. To run the kinetics preprocessor, execute the following steps:

1. Place the chem.inp and therm.dat files into a new folder. This folder will ultimately hold a number of output and diagnostic files.

2. Open a command prompt window running the Intel Fortran/C++ environment.

3. Navigate to the folder you just created using the "cd" command.

4. Type "<chem_path>/chem.exe -i chem.inp -o chem.out -d therm.dat" where <chem_path>is the location of CHEM.exe. This will create chem.out as an output file, which is later read by Senkin and OPPDIF.

OPPDIF requires an additional preprocessing step to fit the transport properties of each species such as thermal conductivity, viscosity, and binary diffusion coefficients. The TRAN.exe program has been modified by Hai Wang to allow for polynomial curve fits for transport properties instead of a more basic formulation that is typically employed. To run the transport preprocessor, complete the following steps:

1. Place the tran.dat file into the folder containing the chem.inp and therm.dat files if you have not done so already. The folder should now also contain chem.out.

2. Open a command prompt window and navigate to the folder as before.

3. Type "<tran_path>/tran.exe -d tran.dat -o tran.out" where <tran_path>is the location of TRAN.exe. This will create tran.out as an output file, which is later read by OPPDIF.

Now preprocessing is complete and Senkin and OPPDIF can be run. Both programs require an input file where inlet conditions, initial grid points, convergence criteria, timestep limits, and other criteria must be specified. The programs read inputs from senkin.inp and oppdif.inp in a keyword format. Consult the Senkin and OPPDIF manuals for a complete listing of keywords and they're meanings. A

working input file for both Senkin and OPPDIF are provided below. To run the programs, complete the following steps:

1. Place the senkin.inp or oppdif.inp file in the folder containing all of the preprocessed files.

2. Open a command prompt window and navigate to the folder as before.

3. Type "<SENKIN_path>/senkin.exe -i senkin.inp -o senkin.out", where <SENKIN_path>is the location of SENKIN.exe. Alternatively, type "<OPPDIF_path>/oppdif.exe -i oppdif.inp -o oppdif.out", where <OPPDIF_path>is the location of OPPDIF.exe. This will create senkin.out or oppdif.out as an output file, which can be post-processed using an external Matlab program.

The OPPDIF program will typically take some time to reach an acceptable convergence level. Continuations are typically performed so the program finds an initial solution to the problem with a very coarse mesh, and then refines the mesh until gradients and curvature are well-resolved. Acceptable levels of GRAD and CURV parameters are found at the end of the sample input file provided in the subsequent section.

F.1   Sample OPPDIF Input File

```
MULT
TDIF
PCAD 0.75
RGTC 1.0
ENRG
PLAT
AFUE 0
AOXI 0
/
/high strain
/VFUE 40
/VOXI 175
/med strain
/VFUE 20
/VOXI 80
/low strain
VFUE 10
VOXI 40
/
TFUE 573
TOXI 1300
TMAX 1700
/
/ Grid setup
NPTS 40
XEND 4.0
XCEN 1.8
WMIX 1.25
/
/
PRES 1.0
IRET 100
UFAC 2.
SFLR -1.E-4
PRNT 1
```

```
TIME 100 5.E-7
TIM2 100 5.E-7
GRAD 0.5
CURV 0.5
FUEL POSF11498 1
OXID N2 0.81
OXID O2 0.06
OXID H2O 0.10
OXID CO2 0.03
/
/ For 9% O2
/PROD H2O 0.158
/PROD CO2 0.0858
/PROD N2 0.7562
/
/ For 6% O2
PROD N2 0.7933
PROD CO2 0.0676
PROD H2O 0.1391
/
/ For 3% O2
/PROD N2 0.8313
/PROD CO2 0.049
/PROD H2O 0.1197
RTOL 1.E-4
ATOL 1.E-7
ATIM 1.E-7
RTIM 1.E-4
/
CNTN
END
/
GRAD 0.2
CURV 0.5
CNTN
END
GRAD 0.1
CURV 0.3
```

```
CNTN
END
GRAD 0.1
CURV 0.1
CNTN
END
GRAD 0.05
CURV 0.05
END
```

F.2   Sample SENKIN Input File

```
CONP
TEMP 1300
REAC POSF11498 1
REAC O2 20
REAC N2 560
REAC CO2 20
REAC H2O 66.67
REAC CH2O 6e-1
PRES 1.0
TIME 2e-2
DELT 1.e-5
DTSV 1.e-4
END
```